

Applications of Frequency Selective Surfaces in Polarization Control of Antennas

by

Farhad Khosravi

A thesis submitted in partial fulfillment of the requirements for the degree of

Master of Science

in

Electromagnetics and Microwaves

Department of Electrical and Computer Engineering
University of Alberta

© Farhad Khosravi, 2014

Abstract

The purpose of this dissertation is to address the problems associated with the current antennas deployed for wireless and navigation purposes. The focus in this work is on the circular polarization radiation of the antennas and the goal is to improve their radiation properties. The methods presented are based on Frequency Selective Surfaces (FSS); a group of periodic structures that behave as a spatial filter in principal but can be adjusted for other alterations to the incident electromagnetic wave. The FSS can be designed adequately so that the transmitted wave undergoes a change in amplitude or phase. Moreover, adding the feature of selectivity over the incident polarization (TE or TM), can make the FSS shape the radiation pattern of the antenna in terms of amplitude or polarization; depending on whether the change is in the amplitude or phase of the wave transmitted through the FSS. The introduction chapter discusses the contemporary problems with these antennas and solution already proposed for these issues. Besides, it discusses drawbacks in current solutions and their limitations in those methods.

The next chapter talks about bidirectional same sense circularly polarized antennas. The effort in this chapter is to present a method, besides those currently presented in literature, to achieve bidirectional antennas which radiate same sense of polarization on the two beams. A multilayer FSS is proposed to change the sense of the polarization by changing the phase of the wave passing through the structure. Then the FSS is combined with the antenna. Axial ratio of better than 3dB is achieved on both sides at the GPS L1 frequency band ($f=1.575\text{GHz}$).

The next chapter is on improving one of the major issues in GPS antennas. Contemporary GPS antennas suffer from high axial ratio at angles close to 90° from the broadside direc-

tion. While there are some antennas available currently, they are either bulky or large in profile. It will be shown that, besides the presumed source of problem in previous works, another intrinsic factor in the radiation equations is also predominantly playing role in the corruption of axial ratio at those angles. Again, the approach presented for the aforementioned problem is based on FSS structures. The FSS will be appropriately designed for different angles to change the amplitude of the transmitted wave through the FSS and then is placed on the antenna. As will be shown, axial ratio is improved to the desired value with the low profile and low cost structure. As the results of this chapter shows, axial ratio of better than 2dB is achieved at angles up to 100° in all of the planes of the radiation pattern. Although the approach is to address one of the problems in the GPS antennas, the methodology seems pretty promising in many other applications where the radiation pattern of the antenna needs to be altered for different angles.

Preface

Chapter 2 of this thesis will be published as F. Khosravi and P. Mousavi "Bidirectional Same Sense Circularly Polarized Slot Antenna Using Polarization Converting Surface", *Antennas and Propagation, IEEE Transactions on*, vol. 13, Issue 1, 2014. I was responsible for analysis, design, measurement, and manuscript composition. P. Mousavi was the supervisory author and was involved with content formation, analysis and also manuscript composition.

Dedicated to My Beloved Parents

Acknowledgements

During all of my efforts in the past years, there have been always precious people who have helped and guided me in my career and, in general, my life. Their patience and support was the essential part of my journey without which none of these effort would result in any achievement.

I owe many thanks my supervisor, Professor Pedram Mousavi, for all of his valuable supports, comments, and suggestions in conducting this project. I would also thank my co-supervisor, Professor Vien Van, for his kind supports and considerations during my M.Sc. period. I also wish to acknowledge my evaluation committee members, Professor Ashwin Iyer and Professor Douglas Barlage. In addition, I would like to thank Pinder Bains for organizing the defense session.

I would take this opportunity to thank my precious group members who have helped me in reaching this point. Among them, Hamid Moghadas is undoubtedly one the most effective ones with his priceless comments, ideas, and supports. Moreover, I would also thank Souren Shamsinejad, Shila Shamsadini, and Fatemeh Mohammadi Monavar for their helpful discussions.

I wish thank TRTech for their great spiritual and financial supports and providing appropriate facilities in doing this project. In addition, I would appreciate the supports from AITF, NSERC, and ITS electronics.

My wonderful friends in Edmonton deserve a special round appreciation for all of their friendships, warm sympathies, and being like a family to me. With them, every moment of my life has been joyful with everlasting memories.

And last but not the least, my best appreciations and acknowledgments goes to my beloved family who have always provided superb and continuous support in the path of all of my progressions towards my destinies. Their presence is the true motivation behind any of my achievements to the time.

My concrete appreciations cannot be expressed in these limited words. These sentences are a small part of the enormous acknowledgement I desire to utter for all of the people who have been on my way. My true appreciation and gratitude goes for them from bottom of my heart forever.

Table of Contents

1	Introduction	1
1.1	Bidirectional Same Sense Circularly Polarized Antennas	4
1.2	Antennas with Low Susceptibility to Multipath Signal at Low Angles	6
1.3	Frequency Selective Surfaces (FSS)	7
1.3.1	Resonant FSS	7
1.3.2	Non-Resonant FSS	9
1.4	Circularly Polarized Antennas	9
1.4.1	Bidirectional CP Antennas	10
1.4.2	Unidirectional CP Antennas	10
1.5	Organization of Thesis	11
2	Implementation of Polarization Converting Surface Using FSS as a Phase Mod- ifier	12
2.1	PCS Design	13
2.1.1	Design Procedure	14
2.1.2	Unit Cell Simulation	16
2.2	Antenna Structure	19
2.2.1	Radiating Element	20
2.2.2	Final Structure	22
2.3	Conclusion	24
3	Implementation of Polarization Selective Surface Using FSS as an Amplitude Modifier	28
3.1	Surface Waves in Patch Antennas	28
3.2	Contribution of Surface Waves to the Far-Field Radiation	30
3.3	Field Radiated by Circular Patch Antenna	33
3.3.1	Cavity Fields	34
3.3.2	Radiated Fields	35
3.4	Frequency Selective Surface Approach	40
3.4.1	FSS Design	40
3.4.2	Tapering procedure of the FSS	42
3.5	CAFSS on Top of The Antenna	45
3.5.1	Implementation	45
3.5.2	Simulation Results	48
3.6	Other Measures of the Antenna	51
3.6.1	Phase Center	52
3.6.2	Up/Down Ratio	54
3.7	Effect of the Size of CAFSS	54
3.8	Effect of Proximity to the Ground	58
3.9	90° Hybrid Phase Shifter	59
3.10	Conclusion	63

4	Conclusion and Future Work	65
4.1	Overall Contributions	65
4.1.1	Bidirectional Same Sense CP Wave Antenna	65
4.1.2	Antennas with Low Susceptibility to Low Angles	66
4.2	Future Research Directions	67
4.2.1	Dual-band Bidirectional Same Sense CP Antenna	68
4.2.2	Dual-band CP Antenna with Low Susceptibility to Low Angles	68
4.2.3	Surface Wave Suppressed Antenna with Improved Axial Ratio	69
4.2.4	Analytical Modeling of CAFSS and FSS Placed Close to the Antenna	69
	Bibliography	71

List of Tables

2.1	Physical properties of unit cell for bottom and top layers	17
2.2	Physical properties of unit cell for the middle layer	17
3.1	Physical properties of non-resonant FSS unit cell	42
3.2	Physical properties of non-resonant FSS unit cell	45
3.3	Parameters of CAFSS	47
3.4	Final parameters of CAFSS	48
3.5	Parameters of CAFSS	56

List of Figures

1.1	Bidirectional Radiation Pattern.	5
1.2	Typical shapes of FSS(Taken from [1]).	8
1.3	An example of Non-resonant FSS (Taken from [2]).	9
2.1	Configuration of proposed structure.	12
2.2	Unit cell configuration of the JC slot PCS	14
2.3	Equivalent network of the JC slot PCS	15
2.4	S_{11} and transmission phase of the equivalent network for arbitrary element values	16
2.5	S_{11} of the PCS for the two linear polarizations along x - and y -directions and normal wave incidence.	17
2.6	S_{21} of the PCS for the two linear polarizations along x - and y -directions and normal wave incidence.	18
2.7	S_{21} phase of the PCS for the two linear polarizations along x - and y -directions and normal wave incidence.	18
2.8	Transmission and reflection coefficients of the PCS for circular polarization incident at normal direction. (inc. , refl., and trans. stand for incident, reflected and transmitted, respectively).	19
2.9	S_{11} of the PCS–LHCP incident, RHCP reflected– for different angles of incidence.	20
2.10	Structure of the radiating element (a) Top view (b) Bottom view.	21
2.11	S_{11} of the antenna alone (a) $W = 82mm$ (b) $W = 90mm$	21
2.12	Normalized radiation pattern of the antenna alone at $1.57GHz$ (a) $W = 82mm$ (b) $W = 90mm$	22
2.13	Antenna structure(a) PCS (b) Antenna (c) Final Structure.	24
2.14	S_{11} of the final structure (a) $W = 82mm$ (b) $W = 90mm$	24
2.15	Normalized radiation pattern at $1.56GHz$ (a) $W = 82mm$ (b) $W = 90mm$	25
2.16	Normalized radiation pattern at $1.57GHz$ (a) $W = 82mm$ (b) $W = 90mm$	25
2.17	Normalized radiation pattern at $1.58GHz$ (a) $W = 82mm$ (b) $W = 90mm$	26
2.18	Axial ratio at $1.56GHz$ (a) $W = 82mm$ (b) $W = 90mm$	26
2.19	Axial ratio at $1.57GHz$ (a) $W = 82mm$ (b) $W = 90mm$	27
2.20	Axial ratio at $1.58GHz$ (a) $W = 82mm$ (b) $W = 90mm$	27
3.1	Grounded Dielectric Sheet	29
3.2	Normalized radiation pattern of circular patch antenna at $1.57GHz$ (a) finite ground plane $W = 250mm$ (b) infinite ground plane.	31
3.3	Axial ratio of circular patch antenna at $1.57GHz$ (a) finite ground plane $W = 250mm$ (b) infinite ground plane.	32
3.4	Circular patch on an infinite ground plane (taken from [3])	33
3.5	Graph of X defined in Equation 3.23	38
3.6	Graph of AR (in dB) given in Equation 3.26	39
3.7	Graph of AR (in dB) given in Equation 3.27	39
3.8	FSS unit cell structure	41

3.9	Equivalent network of the non-resonant FSS (a) dielectric layers modeled by transmission lines (b) transmission lines replaced by lumped element equivalents.	41
3.10	Comparison between the simulation and analytical model of FSS transmission properties for normal incidence.	43
3.11	Expanded view of the FSS in circular arrangement on the antenna.	43
3.12	Electric fields incident on the FSS (a) on RAFSS (b) on CAFSS	44
3.13	Geometry of CAFSS (a) Capacitive layer (b) Inductive layer.	46
3.14	Side view schematic of the CAFSS on the antenna.	46
3.15	Simulation view of the structure with the parameters given in Table 3.3 (a) complete CAFSS (b) first row of CAFSS removed	48
3.16	AR of the structures shown in Figure 3.15 with the tapering parameters given in Table 3.3(a) complete CAFSS (b) first row of CAFSS removed	49
3.17	Ratio of $ E_\theta / E_\phi $ of the structures shown in Figure 3.15 with the tapering parameters given in Table 3.3.	50
3.18	Simulated radiation pattern of the antenna with CAFSS combined with the power divider. Solid lines and dashed lines represent RHCP and LHCP waves, respectively.	51
3.19	Simulated AR of the final structure with the parameters given in Table 3.4.	51
3.20	Ratio of $ E_\theta / E_\phi $ of the final structure with the parameters given in Table 3.4.	52
3.21	$\cos \theta$ profile achieved for the CAFSS used. Dashed line is the $\cos \theta$ function and solid lines are the profiles found by the radiated fields of the antenna at different angles.	52
3.22	Simulation results for the gain of the antenna versus frequency. Solid and dashed lines are the results for the antenna with CAFSS and antenna alone, respectively.	53
3.23	Simulation results for the radiation efficiency of the antenna versus frequency. Solid and dashed lines are the results for the antenna with CAFSS and antenna alone, respectively.	53
3.24	Phase center displacement of the antenna versus frequency.	54
3.25	Multipath with the reflection occurring at the ground.	55
3.26	Up/Down Ratio (UDR) of the antenna evaluated at different angles.	55
3.27	View of the structure with the increased number of rows of CAFSS.	56
3.28	Simulation result for the axial ratio of the structure with increased number of rows in CAFSS.	57
3.29	Simulation results for the radiation pattern of the structure with increased number of rows in CAFSS.	57
3.30	Simulation results for the radiation pattern of the structure with increased number of rows in CAFSS.	58
3.31	Axial ratio of the antenna for different distances from the ground with the size of $2\lambda \times 2\lambda$ (a) $\phi = 0^\circ$ (b) $\phi = 45^\circ$ (c) $\phi = 90^\circ$ (d) $\phi = -45^\circ$	59
3.32	Axial ratio of the antenna for different ground sizes at the distance 2λ away from the antenna (a) $W_g = 2\lambda$ (b) $W_g = 3\lambda$ (c) $W_g = 4\lambda$	60
3.33	Schematic of 90° hybrid (taken from [4]).	60
3.34	90° hybrid in circular shape	61
3.35	Simulation results for the S -parameters of the 90° hybrid shown in Figure 3.34	61
3.36	Transmission phase difference between ports 2 and 3	62
3.37	S -parameters of the 90° hybrid combined with the antenna and CAFSS	62
3.38	Back side view of the final structure; power divider combined with the antenna and CAFSS.	63

List of Symbols

Symbol	Definition	First Use
λ	Free space wavelength	5
E	Electric field	13
k	Wave number	13
ω	Angular frequency	14
Z_0	Characteristic impedance of free space	15
c	Speed of light in free space	29
ϵ_r	Relative permittivity	29
\vec{A}	Magnetic vector potential	34
ϵ	Electric permittivity of a medium	34
μ	Magnetic permeability of a medium	34
f_r	Resonance frequency of circular patch	35

List of Abbreviations

Abbreviation	Description	First Use
CP	Circularly Polarized	1
LH	Left-Handed	1
RH	Right-Handed	1
LOS	Line-of-Sight	1
RHCP	Right-Hand Circularly Polarized	2
LHCP	Left-Hand Circularly Polarized	2
GPS	Global Positioning System	2
FSS	Frequency Selective Surface	2
PRS	Partially Reflective Surfaces	3
PCS	Polarization Converting Surface	6
EBG	Electromagnetic Bandgap Structure	7
SW	Surface Wave	7
RCS	Radar Cross Section	7
JC	Jerusalem Cross	8
AR	Axial Ratio	23
TE	Transverse Electric	29
TM	Transverse Magnetic	29
PEC	Perfect Electric Conductor	33
PMC	Perfect Magnetic Conductor	33
CAFSS	Circularly Arranged Frequency Selective Surface	42
RAFSS	Rectangularly Arranged Frequency Selective Surface	43

PC	Phase Center	51
UDR	Up/Down Ratio	51
SAFSS	Spherically Arranged Frequency Selective Surface	64
LP	Linearly Polarized	66

Chapter 1

Introduction

Many of the contemporary communication systems employ circular polarization for the transmitted signal so as to improve the reliability of the system. More specifically, in the satellite communication, linear polarization undergoes a rotation in the direction of the electric field as it propagates through the ionosphere as a result of Faraday rotation effect [5]. Hence, linear polarization might not be desirable for satellite communication as the direction of the linear polarization plays an important role in the design of antenna for both the receiver and the transmitter. Consequently, the circular polarization is more desirable in satellite communications since it feels only a phase delay and the sense of polarization will be maintained under the Faraday rotation. Moreover, use of circular polarization surpasses the use of complex adjusting systems for antenna alignments in the point-to-point applications like ground based communications. The circularly polarized (CP) wave can be either left-hand (LH) or right-hand (RH) polarized. Most of the applications working based on CP wave deploy only one sense of polarization in the communication of the signal. The primary signal can be diffracted or reflected from the obstacles in the environment before entering the antenna. While the sense of polarization is usually maintained in the diffraction, the sense of polarization is usually changed after being reflected [6]. Hence, some ratio of the multipath signal entering the antenna has a different sense of polarization compared to the line-of-sight (LOS) signal. Since the multipath signal introduces error into the accuracy of the received signal for most of the applications, it is desirable to eliminate the reception of the multipath signal. The multipath problem cannot be completely addressed in the signal processing because the primary and the multipath signals are not usually separated enough in time to be discerned after the reception. Hence, the problem is needed to

be elevated before the reception [7]. Given these issues, it is desirable for a CP antenna to receive only one sense of polarization and reject reception of the other sense of polarization. For instance, an ideal antenna designed to receive Right Hand Circularly Polarized (RHCP) wave, suppresses the reception of Left Hand Circularly Polarized (LHCP) wave from all of the directions. The practical designs, however, suffer from the reception of undesirable polarization from some of the directions.

There are abundant designs available in literature for the resolution of flaws in the radiation pattern of the antennas with the purpose of improvement of reception of desirable wave (Co-polar wave) and rejection of undesirable wave (X-polar wave). Since the solution is dependent on the application and frequency of operation, we focus our attention on Global Positioning System (GPS) application. The designs and procedures, however, are not limited to this application and with appropriate modifications, are applicable to other applications.

While the use of GPS system encompass various applications with different requirements, many of these applications require centimeter or sub-centimeter level of accuracy. Examples include surveying & mapping and also space applications. For such applications, multipath is an important issue in reaching the desired level of accuracy.

The approach in this thesis is to combine the antenna with a periodic structure which can basically be considered as a Frequency Selective Surfaces (FSS) and is used to alter the wave passing through the FSS and at the same time behave as a spatial filter. The changes introduced to the waves can be both to the amplitude or phase of the transmitted wave. For either case, however, a selectivity over the incident polarization will be introduced in order to improve the asymmetries in the radiation pattern by changing the amplitude or phase of the transmitted wave in different ways for each of the polarizations. Depending on the type of changes introduced to the transmitted wave, different applications for various requirements can be extracted. While the conventional use of FSS is in far-field region of the antenna or for plane wave incidence [1], in this thesis, the FSS is placed in the reactive near-field region of the antenna to both keep the structure small and alter the field distribution of the antenna to attain the required radiation pattern.

While the use of FSS with the purpose of modifying the radiation pattern of the antenna is not much common, the approaches discussed in this thesis seems promising in deriving more applications for the antenna designs at different frequency bands. While the general

idea looks similar to the Partially Reflective Surfaces (PRS) , basic principles, applications of use, and also requirements for the design are essentially different. PRS works based on multiple reflection and bouncing of the wave between the PRS and the ground plane of the antenna for the waves generated from a source located on a large ground plane (compared to the wavelength) [8]. For our case, however, the change to the radiated field is obtained by a single transmission of the wave through the FSS. This is due to the fact that the transmission coefficient of the FSS is close to unity for most of the angles of incidence and if any increase in the reflection coefficient is introduced is to reduce the radiation of the antenna in that specific direction. Moreover, for PRS structures, the distance between the antenna and the PRS should be a factor of the wavelength. On the contrary, for the FSS and antenna discussed in this thesis, the distance is usually much smaller than the wavelength ($\sim 0.1\lambda$). This is important for the applications where the wavelength gets significant and smaller size antennas are demanded. Although a reflection coefficient of greater than zero may be required at some directions for a specific polarization – as will be shown later in this dissertation – the FSS will be designed predominately for operation at zero reflection coefficient or around the zero reflection coefficient. For the PRS structures, however, the PRS is needed to be adequately designed to exhibit a nonzero reflection coefficient in order to put the PRS into work. The PRS can also be designed for selectivity over the polarization [9] or may be tapered along the surface of the PRS to demonstrate different reflection coefficients for different angles of incidence [10], but the basic principle of operation is the same as all of the PRS structures. For the PRS structures, one important fact is to design the PRS such that the waves emanate in phase from the PRS after multiple reflections, across the PRS surface [8]. Hence, the PRS is needed to have an area of multiple wavelengths to exhibit the phase distribution across the surface. For the FSS structures combined with the antenna in this thesis, however, the FSS is smaller than a wavelength in area and the required behaviour can be extracted by a few number of FSS unit cells.

With the considerations discussed, this work is focused to address two problems based on the combination of the FSS with the antenna with the selectivity over polarization, as follows in the next sections.

1.1 Bidirectional Same Sense Circularly Polarized Antennas

Bidirectional antennas are those which have a radiation pattern with two major beams on each side of the antenna axis (see Figure 1.1). Maximum radiation occurs at these two beams which are usually located at $\theta = 0^\circ$ and 180° . CP antennas with bidirectional radiation pattern radiate different senses of polarization on each beam. For instance, a CP slot antenna radiates RHCP wave on one side of the antenna and LHCP wave on the other side by nature. Hence, a reflector, is usually placed on one side of the antenna to make the antenna radiate only one sense of polarization [11] in one direction. The size of the ground plane as well as the reflector can be as small as a wavelength up to multiple wavelengths [3, 11]. Since various mobile and indoor applications require bidirectional antennas (e.g. microcellular base station, high-speed WLAN), CP bidirectional antennas with same sense of polarization on each side are required. A portion of this thesis will focus on these antennas. There are currently designs with this property available in literature ([12–17]). References [12–16] are essentially patch antennas attached back-to-back. In order to generate CP polarization, the corner of the antenna can be truncated to generate CP waves as a result of perturbation in the dominant mode of the antenna [3]. Multiple ports can also be used to excite two orthogonal 90 degrees out of phase modes in the patch [3]. This method, however, requires more complex feeding network. In [17] a quite different structure is used to achieve a bidirectional CP antenna. Two inclined metallic strips are placed inside a waveguide and excited 90 degrees out of phase. Although a good axial ratio bandwidth is achieved, the structure is bulky and expensive which makes it unsuitable for many wireless applications.

As stated earlier, in the structures proposed in this thesis, FSS is combined with the antenna to achieve the required radiation pattern. In this work, a slot antenna with bidirectional CP radiation pattern is integrated with an appropriately designed FSS which basically add changes to the phase of the electromagnetic waves passing through the FSS. The FSS is designed so that it changes the sense of CP wave. In other words, if an LHCP wave is incident on FSS the transmitted wave will be RHCP wave and vice versa. There are designs available in literature with the purpose of modification to the polarization of the incident wave. In [18], a linear to circular polarization converter is proposed. The incident wave is decomposed into two perpendicular linear polarizations. Then -45° and $+45^\circ$ phase

shifts are introduced to the linear polarizations as they pass through the FSS. The structure is designed to have the resonance frequency slightly higher and lower the frequency of operation, respectively, to achieve the required phase shifts for the two linear polarizations. Although similar method may be used for the LHCP to RHCP wave conversion by introducing -90^0 and $+90^0$ instead of -45^0 and $+45^0$ phase shifts, this method requires relatively larger bandwidth because the structure works slightly off the resonance frequency. In fact, the structure is needed to work slightly lower and higher than the resonance frequency, respectively, for the two linear polarizations while keeping the transmission properties with the lowest insertion loss. [19] is an FSS with selectivity on only one sense of polarization. In other words, the structure can be designed to transmit the LHCP wave and reflect the RHCP wave. This FSS is composed of two layers of linear to circular polarization converters (similar to the one presented by [18]) and one layer of linear polarizer (which changes the directions of linear polarization). The whole structure results in the propagation of one sense of polarization and reflection of the other sense of polarization of CP wave. Although there are many similar FSS in literature, they basically require unit cells of sizes comparable to the wavelength. Applications at lower frequencies regions (like L-band), however, have constraints on the size of the structure and since at least four unit cells are required to make the FSS operate, unit cells of small sizes compared to the wavelength are required. The FSS proposed in this work, consists of unit cells with the size of about 0.2λ (λ is the free space wavelength) which despite the polarizers discussed earlier, operates at its resonance frequency. The FSS is a resonant FSS in the sense that it demonstrates its transmission properties (total reflection or transmission) using only a single layer of FSS and size of

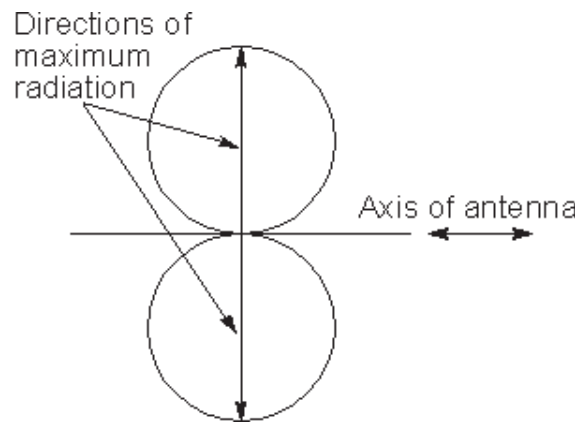


Figure 1.1: Bidirectional Radiation Pattern.

about quarter wavelength. The FSS introduces 0° and 180° phase shift for two perpendicular linear polarizations and consequently changes the sense of CP wave propagating through. In order to introduce 180° phase shift, the FSS is required to have at least two layers of identical structure. In fact, the FSS act as a Polarization Converting Surface (PCS) . Basics of the operation of the PCS will be discussed in the next chapters.

1.2 Antennas with Low Susceptibility to Multipath Signal at Low Angles

In GPS system, RHCP wave is used to transfer signal from the satellite to the receiver antenna. While some applications, like hand-held mobile devices, do not require much accuracy, many applications demand precisions down to centimeter and sub-centimeters in the position of the antenna. There are sources of error playing role in achieving the required level of accuracy in the high-precision GPS. While many of them can be addressed by the signal processing [7], some of them need to be addressed by appropriate design of the system. One of the major sources of error is the multipath signal entering the antenna. In GPS system, position is calculated with the assumption that the direct line signal is entering the antenna. The transmitted signal from the satellite , however, can undergo different reflections before entering the receiving antenna. This in turn can cause error in the determination of the actual location. Signals with single reflection can contribute to a greater value of error compared to the rays with multiple reflections as they will be attenuated in every reflection. One consequence of reflection for CP wave is the change in the sense of polarizations. Hence, the RHCP wave of the satellite will most probably be converted to the LHCP wave as a result of reflection from the obstacles present in the environment. Hence, in order to mitigate the reception of the multipath signal, the receiving antenna is required to reject reception of LHCP wave. CP antennas designed for this purpose meet this requirement for angles up to 50 or 60 degrees off the broadside direction. They, however, suffer from reception of LHCP waves at low angles close to 90 degrees. Since the probability of receiving multipath signal is higher at low angles, efforts have been done to reduce the susceptibility of the antenna to the multipath signal at low angles. Antennas with choke ring ground planes are among the most successful ones in addressing this problem [20,21]; they, however, are bulky and heavy and, besides the production cost, does not meet the requirement of many contemporary applications. In [22], the ground plane is replaced with an

Electromagnetic Bandgap Structure (EBG) ground plane . The structure with EBG ground plane is larger compared to the one with choke ring ground plane. The ground planes proposed by these papers are designed to suppress the Surface Wave (SW) produced by the antenna. In [23] a different method is proposed to suppress the generation of SW. Patch antenna is modified to stop radiating surface wave modes. In all of these papers, it is assumed that the problem is due to the diffraction of SW at the edges of the ground plane and the efforts have been on preventing the SW from reaching the edge of the ground plane.

While SW is partly responsible for the problem, it will be shown that there is other important factor responsible for the increase in susceptibility of the antenna to X-polar wave at low angles. While the problem seems to be intrinsic problem in radiation equations, a solution based on FSS will be proposed in Chapter 3. In the solution presented, FSS will be used to alter the amplitude of the wave that passes through the FSS with the goal of equalization of radiation pattern of the antenna in terms of the amplitude of the two linear polarizations.

1.3 Frequency Selective Surfaces (FSS)

FSS refers to the periodic structures usually in one- or two-dimensional distribution so as to exhibit selectivity over frequency and to behave as spatial filters. Besides the frequency dependency, their behaviour can also be a function of angle of wave incidence and polarization. FSS can get various applications in radomes [1], reducing Radar Cross Section (RCS) [24], polarizers [18], sub-reflectors in parabolic antennas [1], and etc. Based on the basic principles of operation, FSS can be divided into two groups: Resonant versus Non-resonant structures.

1.3.1 Resonant FSS

FSSs are structures that work essentially at their resonance frequency. Resonant FSS refer to the structures which can demonstrate their frequency dependency using a single layer. In other words, a single layer of resonant FSS exhibit resonance frequency. However, they can be used in multilayer configuration. Resonant FSS can be divided into two primary groups; array of patches or slots. Array of patches are metallic shapes in periodic format and can be modeled by electric currents, while slot arrays are periodic arrangement of slots in metallic surfaces and can be modeled by magnetic currents [1]. While these arrays can be designed

to show different behaviours with regards to frequency, array of patches essentially act as band stop filters, in contrast to slot arrays which behave similar to band-pass filters [1]. Since in our application, we require the FSS to be transparent at the desired frequency, arrays of slots are selected to be the main focus of this thesis.

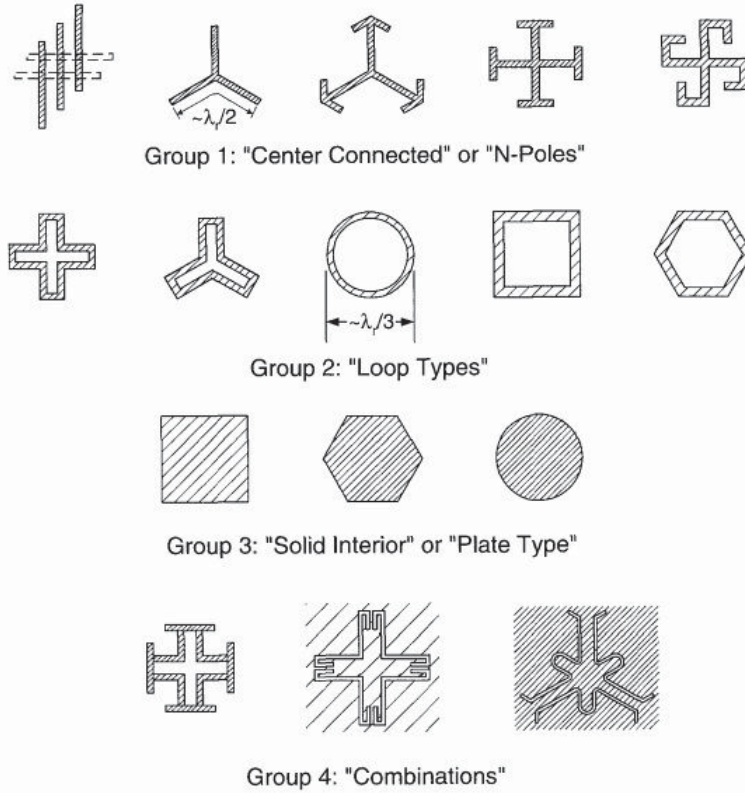


Figure 1.2: Typical shapes of FSS(Taken from [1]).

Figure 1.2 illustrates typical shapes FSS can acquire. While all of these shapes are arrays of patches, complementary shapes of slot type can also be imagined for these shapes. An appropriate selection of the shape of the FSS depend on the application the FSS is being used. For the application we are seeking, since the FSS is required to be placed in close proximity of source, the FSS response is required to be stable with regard to the angle of incidence. Moreover, in order to keep the overall size of the structure as small as possible, the FSS unit cell is preferred to be small. As mentioned earlier, the FSS is used to change the sense of polarization to make the antenna radiate same sense of polarization on both sides. Consequently, the FSS is required to be asymmetric along the two perpendicular axis. Based on these requirements, Jerusalem Cross (JC) shape is selected as it is stable with regard to

the angle of incidence and can be designed separately along two perpendicular axis. The design procedure of the JC slot FSS will be presented in the next chapter.

1.3.2 Non-Resonant FSS

Non-resonant FSS refer to the structures which are composed of capacitive patches and inductive grids on different sides of a substrate which together act as a parallel LC circuit and behave as a first-order band-pass filter (for only one layer of capacitive patch and one layer of inductive grid). The structure is called non-resonant because, unlike the resonant FSSs discussed earlier, constituting elements of the FSS do not exhibit the resonant property at the desired frequency when are isolated from the periodic structure [25]. The simplest example of Non-resonant FSS is the combination of capacitive patches and inductive layers and hence at least two metallic layers are required in order to extract the desired frequency response. Figure 1.3 is an example of non-resonant FSS. One of the advantages to the non-

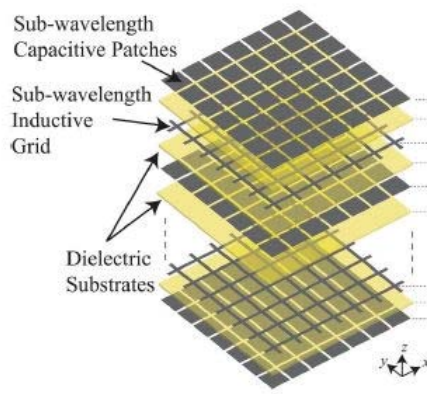


Figure 1.3: An example of Non-resonant FSS (Taken from [2]).

resonant FSSs is their smaller periodicity compared to the resonant FSSs. Moreover, they have simpler design procedure with available analytical model. Details of these FSSs can be found in [26]. Design procedure of these FSSs will be discussed in chapter 3.

1.4 Circularly Polarized Antennas

An appropriate selection of CP antenna, among various available methods for the generation of CP wave, depends on the application and constraints on the structure. In this section, some of the available methods will be presented; divided into two groups of antennas with

bidirectional and unidirectional CP radiation pattern.

1.4.1 Bidirectional CP Antennas

This sub-section discusses antennas which generate bidirectional radiation pattern inherently. However, they can be converted to unidirectional CP antennas by combining the antenna with a reflector placed a quarter-wavelength on one side of the antenna. [11] is an exponentially tapered slot antenna which generates equivalent circular magnetic current on the ground plane of the antenna for CP production. Similar to this antenna, [27] represents a spiral antenna which can be modeled by electric currents on the plane of the antenna. Because of self-complementary shape of these structures, antennas with spiral shape possess larger bandwidth compared to the other types of the antennas and hence are appropriate for wideband or multiband applications. These structures, however, suffer from beam deviation as the frequency goes higher in their bandwidth. To address these problem, they are needed to be made dual-arm which in turn increases the complexity of structure. [28] is an equivalent to monopole antenna with equivalent magnetic currents. In this antenna, a slot is drawn on the corner of the ground plane to generate CP wave and form bidirectional monopole like radiation pattern. Slot antennas have simpler design procedure compared to patch or dipole antennas but are more susceptible to the changes in ground plane and the surrounding environment. For the bidirectional same sense CP antenna designed in this thesis, a slot antenna with a ring shape (similar to the one presented in [29]) is used to get the a bidirectional CP antenna. Details and configuration of the antenna is presented in Chapter 2.

1.4.2 Unidirectional CP Antennas

While bidirectional antennas can be converted into unidirectional antennas by simply placing a reflector on one side of the antenna, there are various other methods for making unidirectional pattern. Microstrip antennas are among the most famous unidirectional antennas which have their main beam at broadside direction (direction perpendicular to the plane of the antenna). A great deal of designs for these antennas can be found in [3]. Patch antenna can be truncated in corner, or a slot can be inserted in middle of the patch to make the antenna generate CP wave. Another method in generating CP antenna is to use an array of two or four patch antennas which are sequentially rotated and the feed position which feed

accordingly to provide appropriate phase between elements. Although this method results in large AR bandwidth and improved AR at lower angles [30], the structure requires large area to place enough number of array elements. The antenna used in this thesis is a simple circular patch antenna excited at two points, 90 degrees out of phase, to generate CP wave. The feeding network is a 90° hybrid phase shifter designed in a circular shape. Details for the design will be presented in Chapter 3.

1.5 Organization of Thesis

This thesis comprises four chapters including introduction. The second chapter introduces the process of changing the phase of the waves radiated by antenna using FSS. Based on this procedure, a bidirectional CP antenna will be designed which radiates the same sense of polarization on two sides of the ground plane of the antenna. This chapter discusses the FSS design and also combination of the FSS with the antenna. An RHCP radiation pattern on both sides of the antenna is achieved with an axial ratio of better than $3dB$ on both sides at 1.56GHz. Chapter three discusses the use of FSS for changing the amplitude of the wave radiated by antenna. This chapter presents the limitations on susceptibility of radiation pattern of GPS antennas to low angles and proposes possible solutions to address those problems. The solution is based on the change in the amplitude of the wave transmitted through the FSS with selectivity over the polarization. Final results for the antenna combined with the FSS will be presented to demonstrate the effectiveness of the approach. The last chapter talks about the future works and possible improvements.

Chapter 2

Implementation of Polarization Converting Surface Using FSS as a Phase Modifier

As discussed in Chapter 1, for many applications deploying CP wave, one sense of polarization is required to transmit signals between the transmitter and the receiver. Hence, for the applications and situations transmitting signal on both sides of the antenna, the existence of a bidirectional CP wave antenna is necessary which radiates same sense of polarization on both sides of the antenna.

In this chapter, the detailed complete study of the work presented in [31,32], a bidirectional CP antenna is realized using a different approach than those presented in the previous chapter. A simple bidirectional slot antenna is combined with a Polarization Converting Surface (PCS) to achieve the same sense of polarization on both sides (See Figure 2.1). The PCS is placed in close proximity of the antenna with the spacing maintained by a layer of foam.

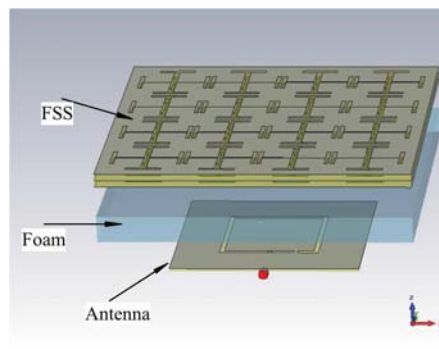


Figure 2.1: Configuration of proposed structure.

The PCS is designed so as to change the sense of the CP wave as it propagates through the PCS by introducing phase changes to the wave. Then, the PCS is placed in close proximity of the slot antenna on the side for which the sense of the polarization needs to be reversed. By placing the PCS on the side with LHCP wave, a bidirectional RHCP antenna can be achieved. The PCS is compatible with all the bidirectional CP antennas. The radiating element, however, has to be adjusted to compensate for the mutual effect of the antenna and the FSS. While the structure is designed for GPS L1 band ($f=1.57$ GHz), the approach can be easily applied to other wireless systems and various radiating structures. The final structure has low fabrication cost and is small compared to the wavelength.

In what follows, first the design procedure of the FSS will be discussed using both analytical and simulation approaches. The design and simulation is for the unit cell of the FSS using periodic boundary condition. The FSS in nature, acts as a PCS to change the sense of the polarization. Then the antenna and an array of 4-by-4 elements of the PCS will be combined together to make the final structures. In this section, the simulation as well as the measurement results of the antenna will be presented. The section 2.3, closes the chapter with the final remarks on this subject.

2.1 PCS Design

Since the goal is to place the PCS in close proximity of the antenna, it is needed to be stable with regard to the angle of incidence. Among various shapes of FSS available in literature [1], those with smaller periodicity have better stability and are of better choice because of the restrictions on the overall size of the structure. Moreover, the FSS has to be transparent at the desired frequency. Given these requirements, JC slot FSS is chosen as described by [1]. The basic operation of the PCS is described by the asymmetric behavior with regard to the incident CP wave decomposed into the two linear polarizations. Assuming an LHCP incident plane wave propagating along the z direction as:

$$\vec{E}^i = E_0(\hat{x} + j\hat{y})e^{-jkz} \quad (2.1)$$

As it will be shown in the next sub-section, the FSS will be designed in order to exhibit 0° and 180° of transmission phase for the two x - and y - directions, respectively. With the introduced phase shifts by the PCS, the transmitted wave can be written as:

$$\vec{E}^t = E_0(\hat{x} - j\hat{y})e^{-jkz} \quad (2.2)$$

which represents an RHCP wave. Since the 180° phase shift cannot be achieved by a single layer, the FSS is chosen to be comprised of three layers of JC slot with two layers of substrates in between. Figure 2.2 shows the unit cell of the JC slot FSS.

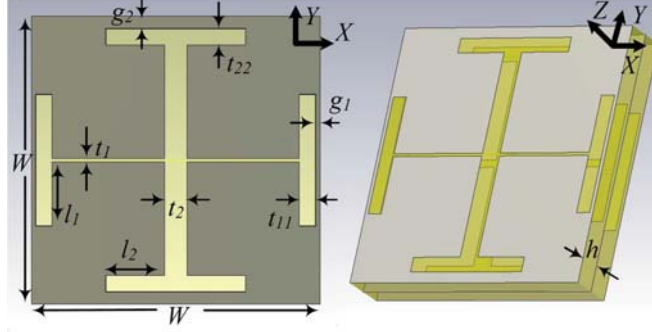


Figure 2.2: Unit cell configuration of the JC slot PCS

2.1.1 Design Procedure

The presented resonant three layer JC slot PCS can be modeled by the lumped element network shown in Figure 2.3 [2]. Since the thickness of the substrates are small compared to the wavelength ($h \sim 0.02\lambda$), the transmission lines can be replaced with their equivalent lumped element networks. As implied in the equivalent network, the two bottom and top layers of the FSS are assumed to be identical. The middle layer, being surrounded by two substrate layers, has a larger capacitance. For the equivalent network presented in Figure 2.3, the following equivalent impedance network parameters can be found:

$$Z_{11} = Z_{22} = \frac{Z_1 Z_3 (Z_2 + Z_1) + Z_1 Z_2 (Z_1 + Z_2 + Z_3)}{(Z_1 + Z_2)(2Z_3 + Z_2 + Z_1)} \quad (2.3a)$$

$$Z_{21} = Z_{12} = \frac{Z_1 Z_3 Z_5}{(Z_1 + Z_2)(2Z_3 + Z_2 + Z_1)} \quad (2.3b)$$

Where

$$Z_1 = \frac{1}{j\omega C_1 + 1/j\omega L} \quad (2.4a)$$

$$Z_2 = j\omega L' \quad (2.4b)$$

$$Z_3 = \frac{1}{j\omega C_2 + 1/j\omega L} \quad (2.4c)$$

S -parameters of the structure, for the given Z_{11} and Z_{21} can be found as [4]:

$$S_{11} = \frac{(Z_{11} - Z_0)(Z_{22} + Z_0) - Z_{12}Z_{21}}{\Delta Z} \quad (2.5a)$$

$$S_{21} = \frac{2Z_{21}Z_0}{\Delta Z} \quad (2.5b)$$

Where $\Delta Z = (Z_{11} + Z_0)(Z_{22} + Z_0) - Z_{12}Z_{21}$ and Z_0 is the characteristic impedance of free space for the plane wave . Figure 2.4 demonstrates the transmission properties for the given equivalent network with arbitrary values of capacitances and inductances. Values of capacitors and inductors in the equivalent network are chosen so as to demonstrate the general transmission properties of the equivalent network only and do not represent any relation with the JC slot PCS parameters. The frequency has been normalized to f_0 where $f_0 = 1/2\pi\sqrt{LC_1}$. L' can be found to be $L' = \mu_0 h$ [2]. For our application, since the thickness of the substrates are fixed ($h = 3.175mm$), value of L' is set to $3.95nH$ to derive the curves in Figure 2.4. C_2 can be manipulated to adjust the transmission phase at the resonance frequencies. In the derivation of Figure 2.4, C_2 is set to be $1.54C_1$.

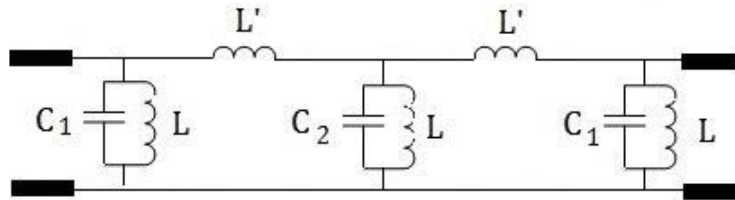


Figure 2.3: Equivalent network of the JC slot PCS

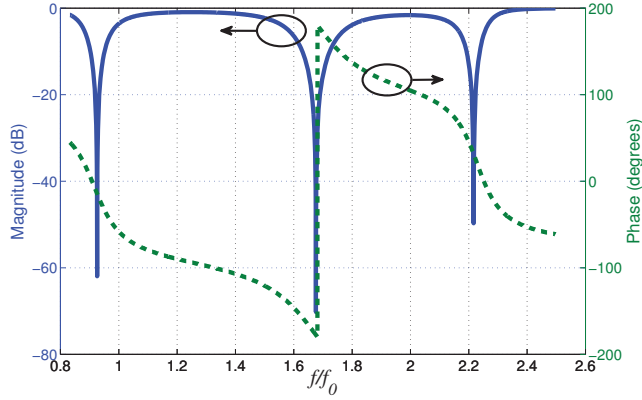


Figure 2.4: S_{11} and transmission phase of the equivalent network for arbitrary element values

As shown, the network exhibits 0° and 180° transmission phase at the first and second resonance frequencies, respectively. The capacitance of the middle layer can be manipulated to adjust the transmission phase at the resonance frequency. To achieve the change in the sense of CP wave propagating through the PCS, the unit cell is needed to be designed so that the first and the second resonances occur for the two perpendicular polarizations simultaneously at the frequency of operation. Consequently, the unit cell would have different configurations with respect to x - and y -directions. In the next sub-section, the unit cell simulation of the PCS will be presented.

2.1.2 Unit Cell Simulation

With the considerations given in the previous sections, the unit cell has been designed for the L1 GPS frequency band. Although there is an analytical model available for the JC FSS [33], tuning has been performed to obtain the parameters since the structure is asymmetric and cannot be designed independently for the two x and y polarizations. In addition, since the structure includes three layers of JC slot, it would have a sophisticated design process based on the analytical method since we should also account for the mutual coupling between different layers. Hence, simulation is performed in CST Microwave Studio with the unit cell boundary conditions. The unit cell boundary condition repeats the structure virtually along the two directions of structure and assigns ports with Floquet modes to the open boundaries. Unit cell parameters for different layers are given in Tables 2.1 and 2.2 with the parameters defined in Figure 2.2. The substrates are TMM4 Rogers materials with

the relative permittivity of 4.5.

Parameter	W	t_1	t_{11}	t_2	t_{22}
Value	35mm	0.4mm	2mm	2.7mm	2mm
Parameter	l_1	g_1	l_2	g_2	h
Value	8mm	1mm	8.5mm	3mm	3.175mm

Table 2.1: Physical properties of unit cell for bottom and top layers

Parameter	W	t_1	t_{11}	t_2	t_{22}
Value	35mm	1mm	2mm	2.7mm	2mm
Parameter	l_1	g_1	l_2	g_2	h
Value	8mm	1mm	8.5mm	3mm	3.175mm

Table 2.2: Physical properties of unit cell for the middle layer

As a result of mutual coupling between the PCS and the antenna, the resonance frequency of the PCS will shift down. To have the resonance occur at $f = 1.57\text{GHz}$, the PCS is designed for $f = 1.62\text{GHz}$. Figure 2.5 and 2.6 demonstrate S_{11} and S_{21} of the PCS, respectively, for linear polarization normal plane wave incidence. The blue and black curves represent the data for the linear polarizations along x - and y -directions, respectively. As shown, the PCS exhibit its first resonance at 1.62GHz for the x -directed linear polarization and its second resonance for the y -directed linear polarization. Transmission phase of the PCS for the

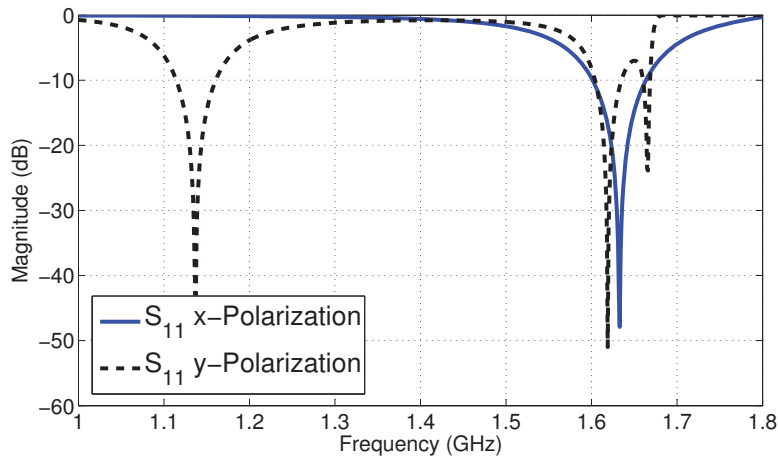


Figure 2.5: S_{11} of the PCS for the two linear polarizations along x - and y -directions and normal wave incidence.

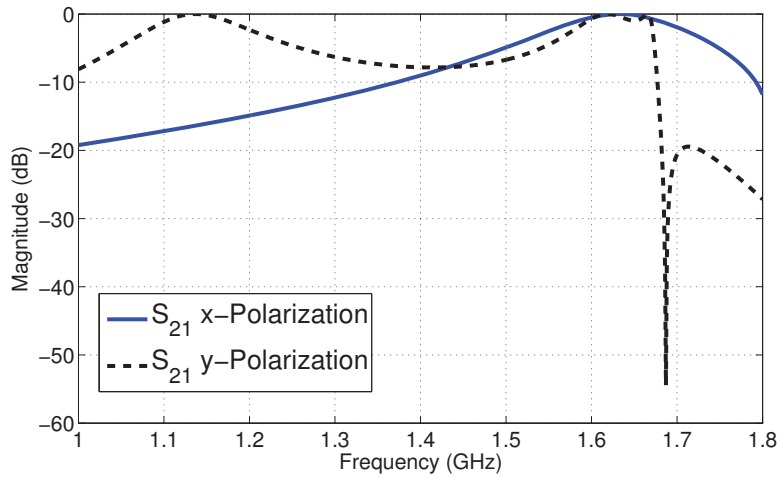


Figure 2.6: S_{21} of the PCS for the two linear polarizations along x - and y -directions and normal wave incidence.

two linear polarizations are shown in Figure 2.7. At 1.62GHz, transmission phase of 0° and 180° occurs for x and y polarizations, respectively. Consequently, as stated earlier, the PCS is expected to change the sense of polarization for the CP wave incidence.

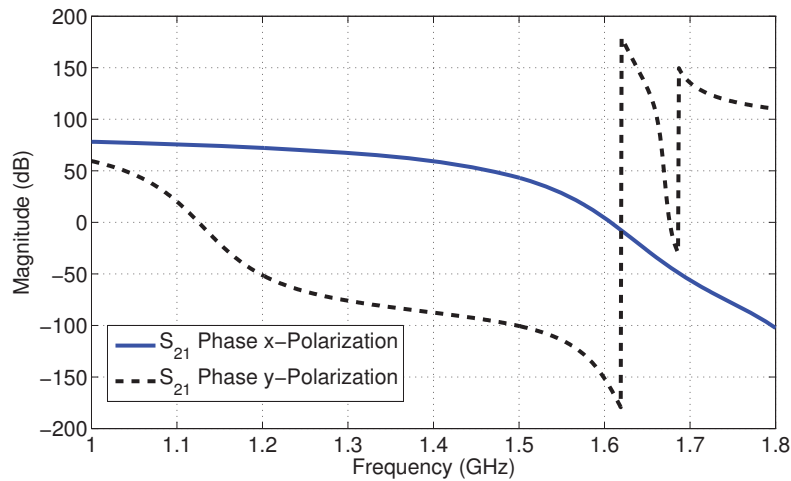


Figure 2.7: S_{21} phase of the PCS for the two linear polarizations along x - and y -directions and normal wave incidence.

Figure 2.8 demonstrates the PCS behavior for CP wave incident at normal direction. The blue solid line indicates the RHCP wave reflection versus LHCP wave incidence. The black dashed line indicates RHCP wave transmission for LHCP wave incidence. In other

words, when LHCP wave is illuminated on the PCS, the transmitted wave is an RHCP wave. It can be inferred that the PCS behaves the same way with regard to the RHCP wave incidence. Figure 2.9 indicates the dependence of PCS on the angle of incidence for the simulated unit cell of the FSS using periodic boundary condition. The wave is incident at angle θ and collected at angle $-\theta$. As shown, the structure is stable with regard to the angles of incidence and can be appropriately placed in vicinity of the antenna.

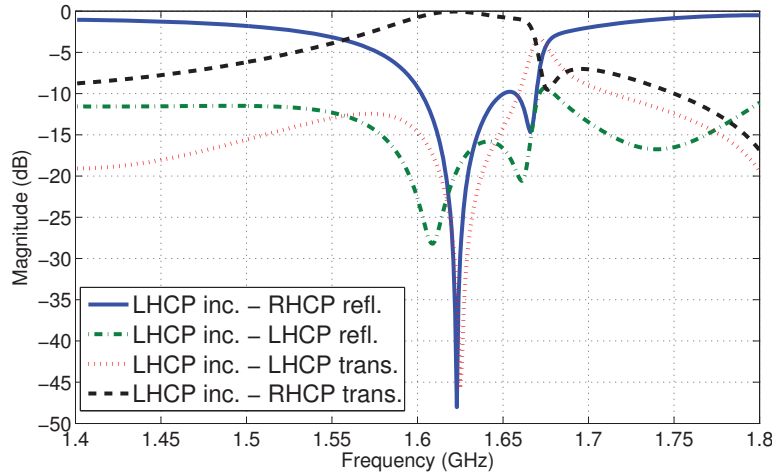


Figure 2.8: Transmission and reflection coefficients of the PCS for circular polarization incident at normal direction. (inc. , refl., and trans. stand for incident, reflected and transmitted, respectively).

In the next section, simulation and measurement results will be presented for the PCS combined with the antenna.

2.2 Antenna Structure

This section demonstrates the final structure of the antenna. First, the radiating element will be presented then the final structure, combined with the PCS, will be shown. This section also compares the measurement and simulation results for both the antenna alone and the final structure. The structure is simulated using CST Microwave Studio. The unit cell of the PCS is simulated using unit cell boundary condition of the software. Frequency Domain Solver is used for the unit cell simulation. Then an array of 4-by-4 of the unit cells is combined with the antenna and the structure is simulated using the Time-Domain Solver. Antenna parameters are optimized for the best reception of RHCP wave and rejection of

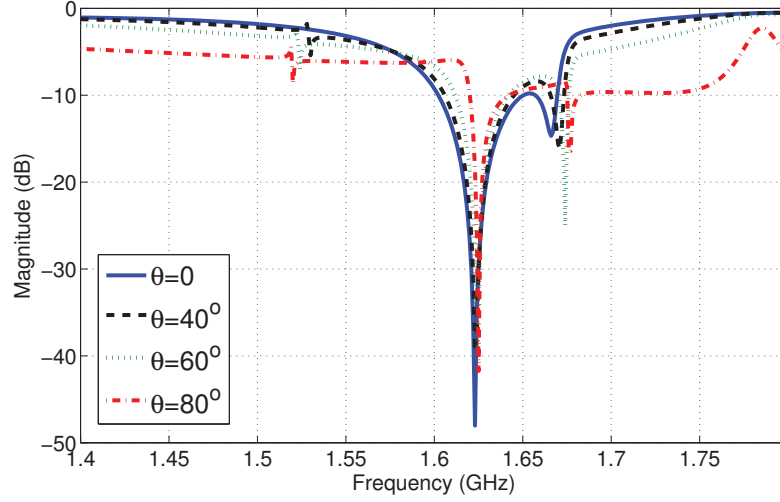


Figure 2.9: S_{11} of the PCS–LHCP incident, RHCP reflected– for different angles of incidence.

LHCP wave at the two main beam directions (i.e. $\theta = 0^\circ$ and $\theta = 180^\circ$).

2.2.1 Radiating Element

A simple ring slot antenna is used as the radiating element . Antenna is excited by a microstrip line and is designed to radiate LHCP wave on the metallic side and RHCP wave on the feed side (Figure 2.10). TMM4 Rogers material is used as the substrate. Width of the square ring and width of the slot are 45.5mm and 2.2mm, respectively. A junction with the width of 2mm is located 13mm off the center of the ring across the slot to generate the circular polarization. The width of the square ring is chosen so that its circumference is about one wavelength. The structure is designed for two different ground plane sizes to illustrate the effect of the ground plane on the radiation properties. Figure 2.11 demonstrates the measured and simulated result of S_{11} of the antenna alone for $W = 82mm$ and $W = 90mm$ where W is the width of the ground plane. Normalized radiation pattern of the antenna for two different ground plane sizes are shown in Figure 2.12. Good agreement between the simulation and measurement results has been achieved. Since the antenna is designed to have the desired radiation pattern when combined with the PCS, the radiation pattern of the antenna alone does not need to necessarily meet the standard requirements of GPS system. Consequently, the antenna parameters are derived with the PCS present in close proximity. To keep the final structure as small as possible, the PCS is placed in

the reactive region of the antenna. Hence, presence of the PCS has a great effect on the radiation properties as well as resonance frequency of the antenna.

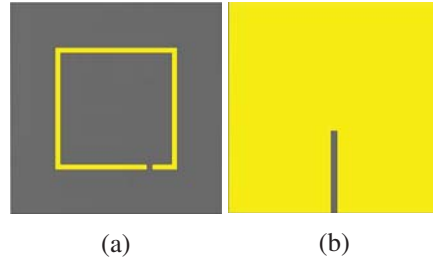
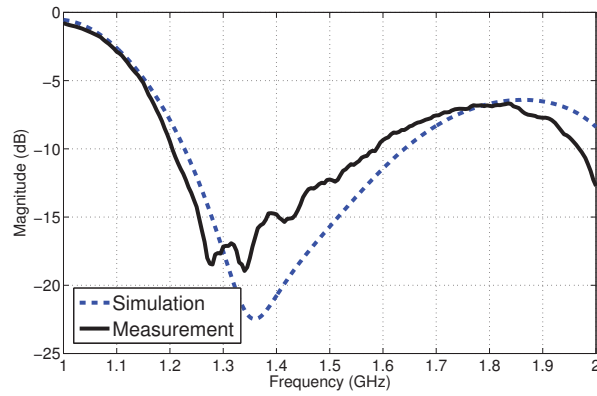
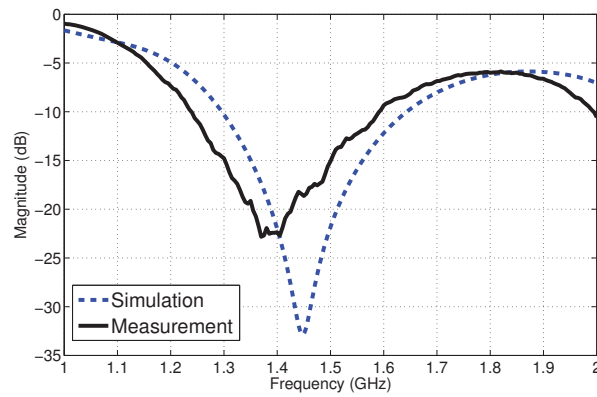


Figure 2.10: Structure of the radiating element (a) Top view (b) Bottom view.

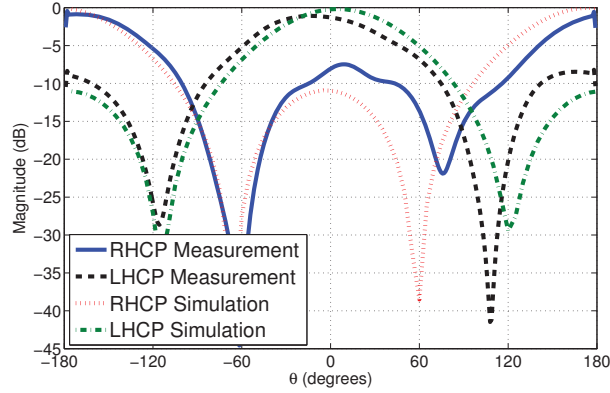


(a)

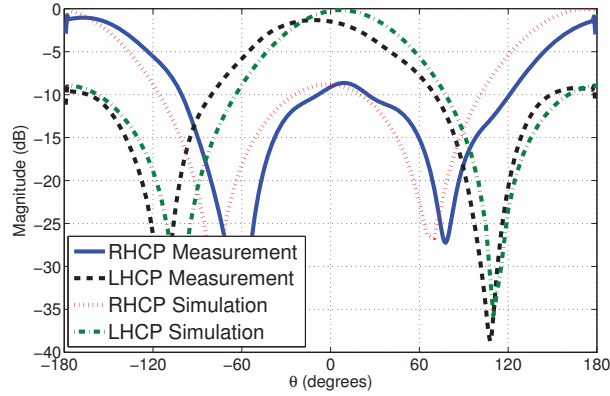


(b)

Figure 2.11: S_{11} of the antenna alone (a) $W = 82mm$ (b) $W = 90mm$.



(a)



(b)

Figure 2.12: Normalized radiation pattern of the antenna alone at 1.57GHz (a) $W = 82\text{mm}$ (b) $W = 90\text{mm}$.

2.2.2 Final Structure

Figure 2.13 demonstrates the final structure. A layer of foam ($r = 1.01$) with the thickness of 1.27mm is inserted between the antenna and the PCS to maintain a uniform spacing between slot antenna and the PCS. For the antenna discussed in the previous section, the boundary of the reactive near-field region of the antenna will be a sphere with a radius of about 32mm surrounding the antenna. Hence, it can be concluded that the PCS is in the reactive near-field region of the antenna. S_{11} of the antenna is depicted in Figure 2.14. The mismatch between the simulation and measurement results of the antenna can be explained by the fact that antenna is a bidirectional slot antenna. The PCS is placed close to the antenna which can greatly affect its properties. Consequently, the structure is sensitive to

its surrounding area and close objects can change the input impedance of the antenna and hence, the behaviour given in the S_{11} of antenna can be expected. This is also evident in the simulation results of Figures 2.14a and 2.14b for a small change in the ground plane size of the antenna. As these curves suggest, ground plane size of the slot antenna is a sensitive parameter and placing the PCS close to the antenna can affect the effective size of the ground plane by extending the fringing fields of the ground plane edges. Input impedance of antenna, however, follows the simulation results for the frequencies around the resonance frequency of PCS (i.e. 1.575GHz). Figures 2.15 through 2.17 show the normalized radiation pattern of the antenna for $W = 82mm$ and $W = 90mm$ at three different frequencies. As shown, the antenna radiates RHCP wave on both sides of the ground planes. Axial ratio (AR) is a number, always greater than one, describing how good a wave is CP. For an elliptically polarized wave, in general, the curved traced by the electric field vector over time is an ellipse. AR is defined as the ratio of major axis to the minor axis of this ellipse and can be written as [3]:

$$AR = \frac{\text{major axis}}{\text{minor axis}} = \frac{OA}{OB} \quad (2.6)$$

where

$$OA = \left[\frac{1}{2} \left\{ E_{\theta 0}^2 + E_{\varphi 0}^2 + [E_{\theta 0}^4 + E_{\varphi 0}^4 + 2E_{\theta 0}^2 E_{\varphi 0}^2 \cos(2\Delta\phi)]^{1/2} \right\} \right]^{1/2} \quad (2.7a)$$

$$OB = \left[\frac{1}{2} \left\{ E_{\theta 0}^2 + E_{\varphi 0}^2 - [E_{\theta 0}^4 + E_{\varphi 0}^4 + 2E_{\theta 0}^2 E_{\varphi 0}^2 \cos(2\Delta\phi)]^{1/2} \right\} \right]^{1/2} \quad (2.7b)$$

$$E_{\theta 0} = |\vec{E}_{\theta}| \quad (2.7c)$$

$$E_{\varphi 0} = |\vec{E}_{\varphi}| \quad (2.7d)$$

where E_{θ} and E_{φ} are far-field radiated electric fields along $\hat{\theta}$ and $\hat{\varphi}$ directions of spherical coordinate system. $\Delta\phi$ is the phase different between the two E_{θ} and E_{φ} components. As the figures for the axial ratio demonstrate (2.18, 2.19, and 2.20), the best response is achieved at 1.56GHz for $W = 82mm$ with axial ratios of 1.83dB and 2.88dB at $\theta = 0^\circ$ and $\theta = 180^\circ$, respectively. High value of AR occurs at about $\theta = 90^\circ$ and $\theta = -90^\circ$

or equivalently on the sides of the ground plane of the antenna where the gain of the antenna drops significantly and antenna basically radiates linear polarization. The mismatch between the measurement and simulation results is due to the uncertainties in setting up the antenna in the chamber and probe errors. The probe is a wideband probe covering the L-band and far-field results are taken from the near-field measurements.

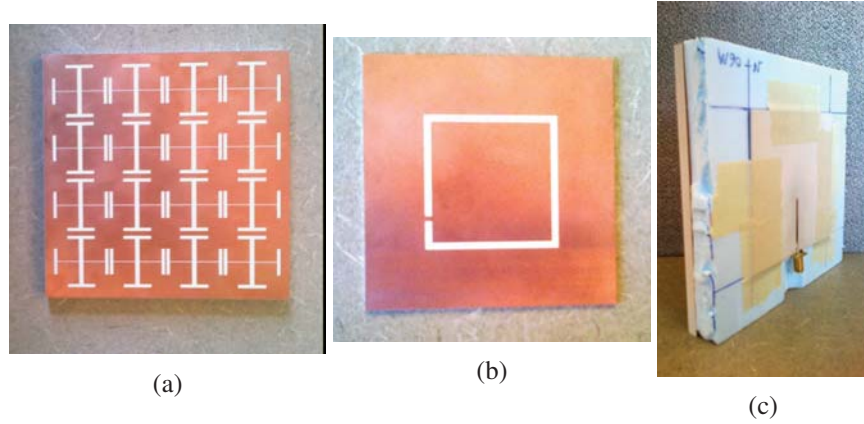


Figure 2.13: Antenna structure(a) PCS (b) Antenna (c) Final Structure.

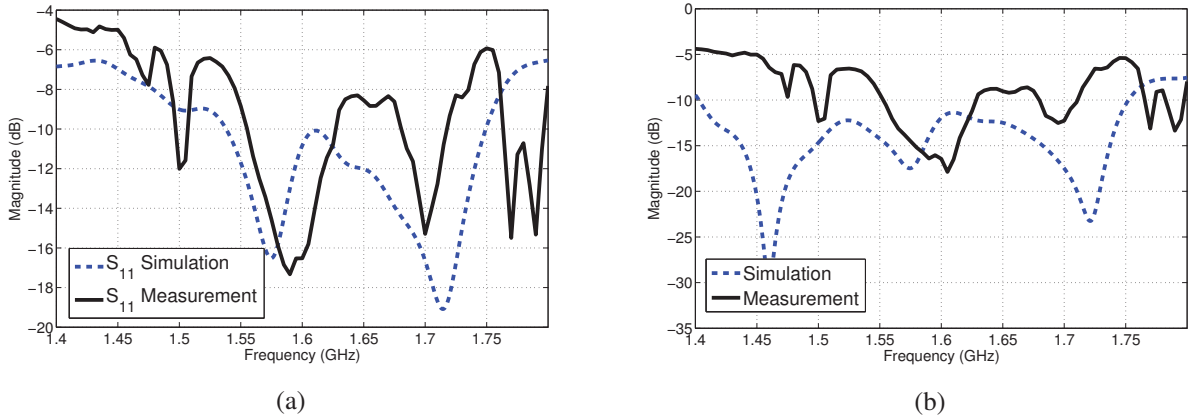


Figure 2.14: S_{11} of the final structure (a) $W = 82mm$ (b) $W = 90mm$.

2.3 Conclusion

In this chapter, a bidirectional CP antenna was proposed. The antenna radiates RHCP wave on both sides of the ground plane. Since the antenna is a bidirectional low gain antenna (gain of about $2dB$ on each side) at low frequencies, the measurements can be done more

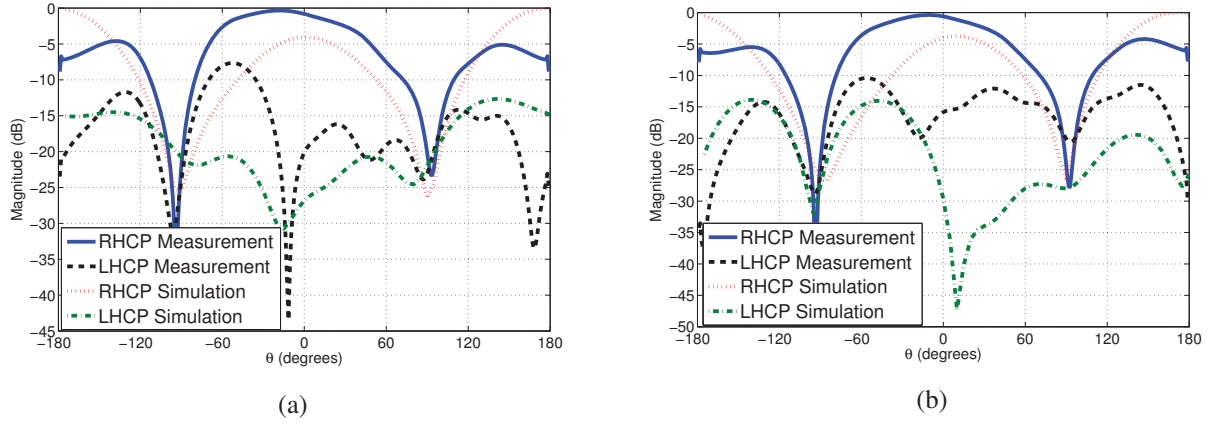


Figure 2.15: Normalized radiation pattern at 1.56GHz (a) $W = 82\text{mm}$ (b) $W = 90\text{mm}$.

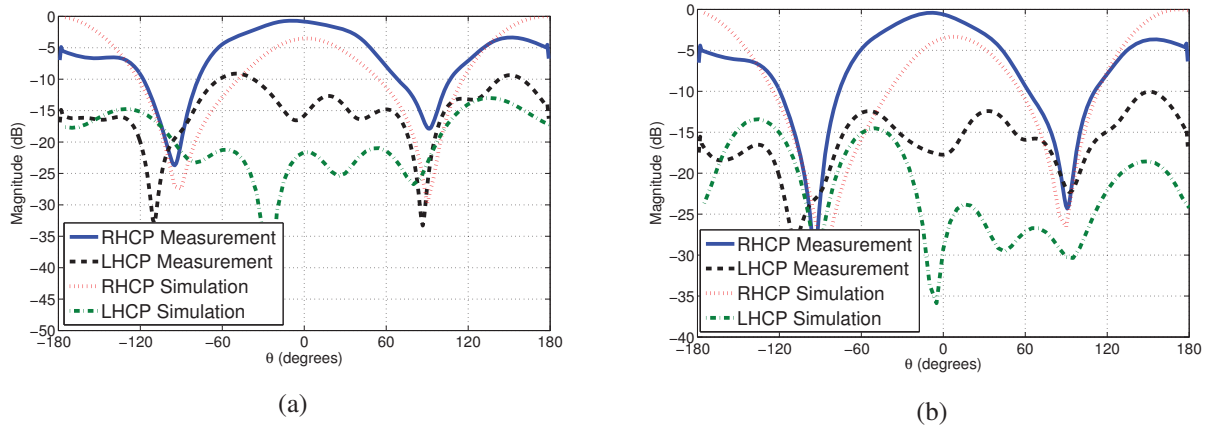
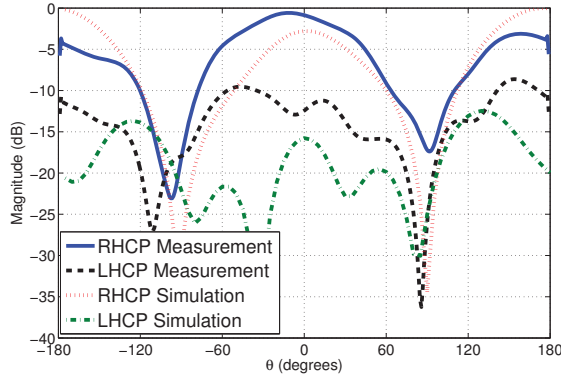
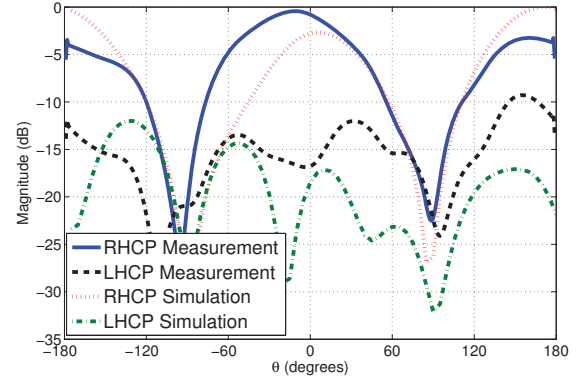


Figure 2.16: Normalized radiation pattern at 1.57GHz (a) $W = 82\text{mm}$ (b) $W = 90\text{mm}$.

accurately in a more sophisticated chamber with a probe designed for L-band measurements. The results, however, demonstrate sufficient match with the simulation results as well as design goals. Hence, the structure can be deployed adequately for the applications requiring bidirectional CP wave antenna. The presented PCS was combined with the square ring slot antenna. The PCS, however, is not limited to this specific antenna and can be integrated into other shapes of slot antennas or other kinds of bidirectional antennas. The antenna parameters, however, are needed to be adjusted for the case when the PCS is placed by the antenna because the PCS is in reactive region of the antenna and hence has an obvious effect on the input impedance as well as radiation properties of the antenna. While the antenna is designed for the GPS L1 band, the procedure can be extended to other frequency

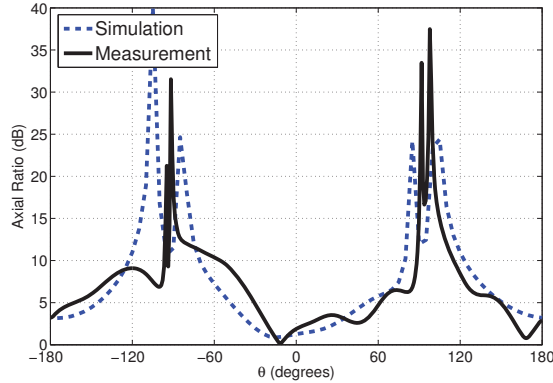


(a)

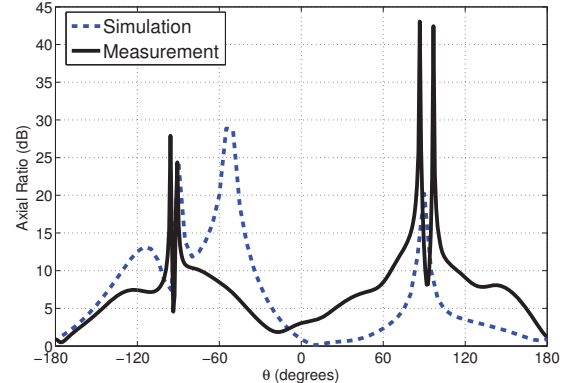


(b)

Figure 2.17: Normalized radiation pattern at 1.58GHz (a) $W = 82mm$ (b) $W = 90mm$.



(a)

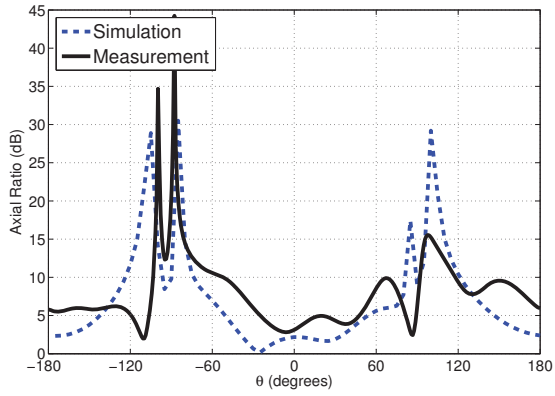


(b)

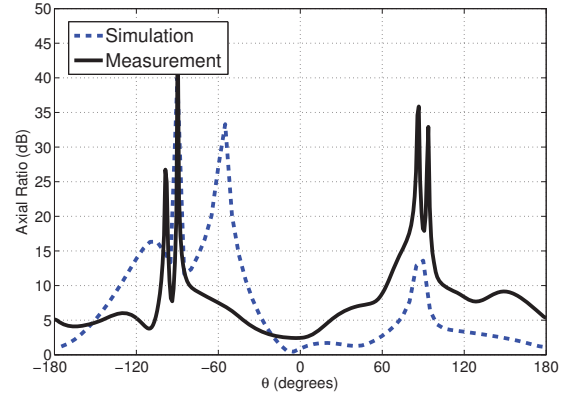
Figure 2.18: Axial ratio at 1.56GHz (a) $W = 82mm$ (b) $W = 90mm$.

ranges.

The application of this PCS is not limited to CP wave. Since the PCS introduces 0° and 180° phase shift for the two perpendicular linear directions, it can also affect a linearly polarized wave. With the incident linearly polarized wave inclined over the PCS with equal components along the two perpendicular directions of PCS, the transmitted wave will be still linearly polarized but with the direction of polarization rotated by 90 degrees. Future works of this chapter will be discussed in more details in the last chapter.

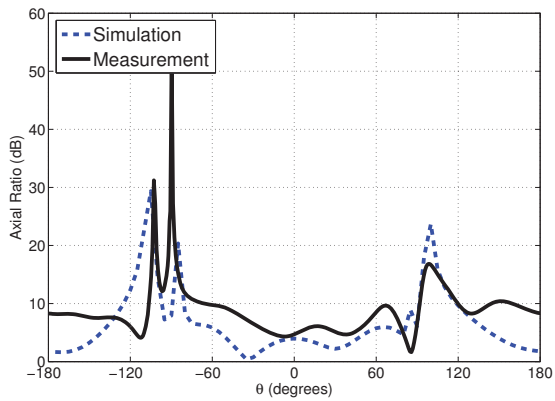


(a)

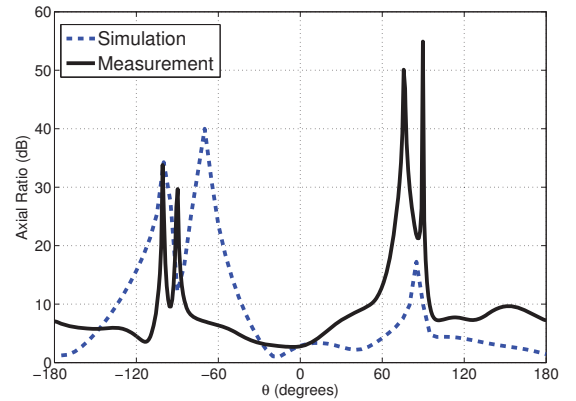


(b)

Figure 2.19: Axial ratio at 1.57GHz (a) $W = 82mm$ (b) $W = 90mm$.



(a)



(b)

Figure 2.20: Axial ratio at 1.58GHz (a) $W = 82mm$ (b) $W = 90mm$.

Chapter 3

Implementation of Polarization Selective Surface Using FSS as an Amplitude Modifier

The goal of this chapter is to address one of the major problems of GPS antennas which causes error in the accurate evaluation of location of the receiving antenna. As discussed in Chapter 1, multipath signal entering the antenna is one of the major sources of error for centimeter to sub-centimeter measurements in the GPS system. Efforts have been made on reducing the susceptibility of the antenna to the multipath signals. Since the multipath signal has usually the opposite sense of polarization compared to the primary signal, the goal in these efforts is to improve the reception of Co-polar wave (RHCP in GPS system) and reject reception of X-polar wave (LHCP wave in GPS wave). It is equivalent to improve the AR of the antenna (with AR defined by 2.6 and 2.7). Since GPS antennas are more sensitive at low angles (angles close to $\theta = 90$ degrees), and because the reception of multipath signal is more probable at low angles, it is desirable to improve the AR of the antenna at low angles. In this chapter, we will first discuss the effects and methods of generation of SWs in the substrates of patch antennas; the source which is assumed to be the main cause of the corruption of AR at low angles. Second, other possible source of increase in AR will be discussed followed by simulation results.

3.1 Surface Waves in Patch Antennas

SWs are referred to as the waves that propagate along an interface of two mediums with different electrical properties. The wave is bound to the surface and propagates along the

boundary of the two mediums. The wave, however, decays exponentially away from the boundary into the mediums [34]. One of the usual interfaces is a grounded dielectric sheet (see Figure 3.1). It is the case for the patch antennas which can support propagation of both TE (Transverse Electric) and TM (Transverse Magnetic) SW modes.

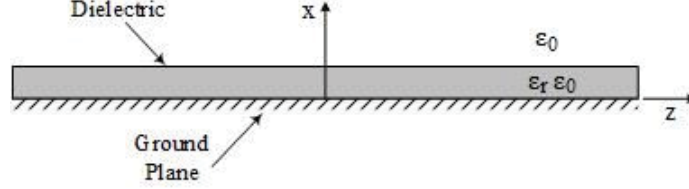


Figure 3.1: Grounded Dielectric Sheet

For the geometry shown in Figure 3.1, the cutoff frequency for the TM SW mode can be written as [4]:

$$f_{c,n} = \frac{nc}{2d\sqrt{\epsilon_r - 1}}, \quad n = 0, 1, 2, \dots \quad (3.1)$$

and for the TE mode as [4]:

$$f_{c,n} = \frac{(2n - 1)c}{4d\sqrt{\epsilon_r - 1}}, \quad n = 1, 2, 3, \dots \quad (3.2)$$

where c , d , and ϵ_r are speed of light in free space, thickness of the dielectric, and relative permittivity of dielectric, respectively. As these equations show, the dominant SW mode for this structure is TM_0 mode with zero cutoff frequency. For dielectric thicknesses on the order of 1mm, and for substrates with the permittivities we are aiming (less than 5), cutoff frequency for the next mode will be around 20 GHz which is far above the operating frequency of GPS L1 band. Hence, it can be assumed that the only existing SW mode for the GPS patch antennas is the TM_0 mode. So we focus on this surface mode only.

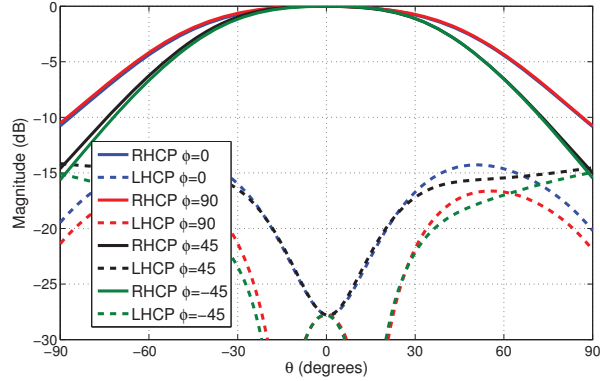
At lower frequencies, where the thickness of the dielectric is small compared to the wavelength, the effect of the dielectric is negligible and hence the dispersion diagram of the TM_0 mode follows a quasi-TEM mode and propagates at a speed very close to the speed of light in free space. At higher frequencies, where the thickness of the substrate gets significant compared to the wavelength, the fields get more confined in the dielectric region and

hence the speed of wave get more closer to the speed of the wave in the dielectric region. Consequently, as we move from zero frequency to the higher frequencies, the propagation constant of the surface wave changes from k_0 (wave number of a plane wave in free space) to the asymptotic value of $\sqrt{\epsilon_r}k_0$ where ϵ_r is the relative permittivity of the dielectric region [34]. Hence, because the speed of propagation for this surface mode is always less than the speed of wave in free space, they cannot provide the phase matching condition with the plane waves in free space and consequently do not couple to plane wave radiation and thus will not radiate unless they reach a discontinuity or surface roughness. At our frequency of focus (GPS L1 band), the thickness of the substrate is small compared to the wavelength (1.57mm compared to 200mm) and thus these surface waves propagate at speed close to the speed of light in free space. Therefore, a small perturbation can make the waves radiate. Radiation of surface waves and also currents propagating on the ground plane of the antenna cause ripples in the radiation pattern and affect the efficiency of the antenna in terms of AR. These effects are more evident for the structures which have larger ground planes compared to the operating wavelength. It is assumed that fields radiated by these surface waves are the main cause of increase in the reception of cross-polarization. Hence, there has been efforts in literature to prevent these waves from propagating and also reaching the edges of the structure [20–23]. In [20–22], ground planes with periodic configuration is presented. These ground planes exhibit band-gap at the frequency of operation and hence prevent propagation of surface wave along the boundary of substrate. In [23], surface wave fields radiated by a circular patch is derived, and using those equations, a condition is derived in order to suppress the generation of surface waves by the antenna. In this dissertation, however, instead of proceeding with the suppression of surface waves, contribution of diffracted surface waves to the far-field cross-polarization reception of radiation pattern will be studied.

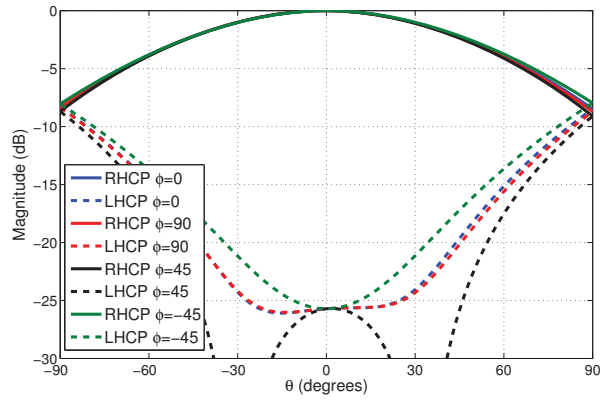
3.2 Contribution of Surface Waves to the Far-Field Radiation

Circular patch antenna is chosen as the primary radiator in this thesis for the sake of simplicity and symmetry of the structure. A simple circular patch antenna is simulated using CST MWS software. The patch is excited at two points 90° apart and 90° out of phase to generate circular polarization [3]. The antenna is simulated for two cases of finite and infi-

nite ground planes. Antenna is simulated on FR-4 substrate with the relative permittivity of 4.3. The thickness of the substrate is 1.016mm and radius of the circular patch is 25.5mm. Figures 3.2 and 3.3 compare the radiation pattern and axial ratio of the two antennas. The ground plane size for the antenna with finite ground plane is $25cm \times 25cm$ ($\sim \lambda \times \lambda$).



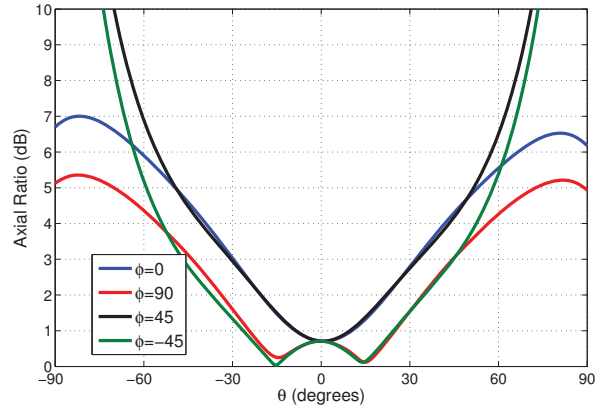
(a)



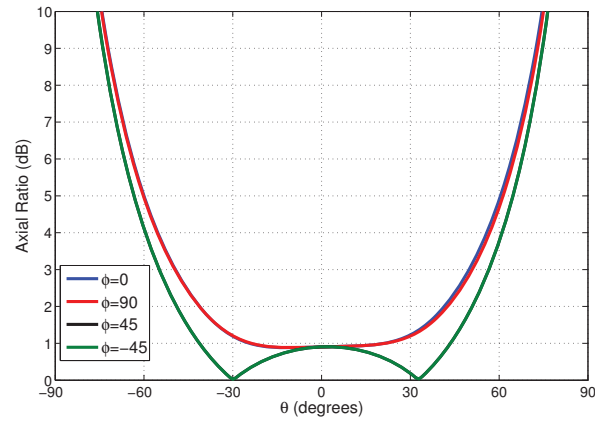
(b)

Figure 3.2: Normalized radiation pattern of circular patch antenna at $1.57GHz$ (a) finite ground plane $W = 250mm$ (b) infinite ground plane.

The only difference between the two antennas is their ground plane sizes. Hence, since the SWs radiate primarily when they reach the edges of the ground plane, it can be concluded that the difference in their radiation pattern is mainly due to the contribution of surface wave radiation. As shown in the radiation pattern of the antennas, although contribution of SWs is evident, the antenna with infinite ground plane still suffers from the reception of X-polar wave at low angles. In other words, even preventing the SWs from radiating, does not guarantee an axial ratio of better than $2dB$ at low angles and the axial ratio is



(a)



(b)

Figure 3.3: Axial ratio of circular patch antenna at 1.57GHz(a) finite ground plane $W = 250mm$ (b) infinite ground plane.

still needed to be reduced further at angles close to 90 degrees. It is worthy to point out that the size of the ground plane has a direct effect on the axial ratio of the antenna. The reason can be due to the fact that the size of the ground plane of the antenna is comparable to the wavelength and a slight change to the size of the ground plane will change the way edge diffracted SWs contribute to the primary fields radiated by the patch. The size of finite ground plane presented here is not optimized for the best AR profile. As Figure 3.2b shows for the antenna on infinite ground plane, at 90° , antenna receives RHCP and LHCP waves equally. In other words, the polarization of the antenna is linear. It can be explained by the fact that because of the infinite ground plane of the antenna, the ϕ component of the radiated field is parallel to the ground plane and thus will be suppressed as a result of boundary

condition imposed to the tangential fields on a conductor. Thus the poor AR is expected at these angles; apart from considering surface wave contributions. This problem will be discussed more quantitatively in the next section.

Although the ground plane of the antenna does not impose linear polarization at $\theta = 90^\circ$ for the antenna on the finite ground plane, the problem still exists to some extent as it is evident in its radiated fields in Figure 3.2a.

In the next section, the problem will be reviewed from another point of view and a solution based on FSSs will be presented.

3.3 Field Radiated by Circular Patch Antenna

In this section, fields radiated by a simple circular patch antenna will be analyzed. Cavity model will be used to evaluate the fields of a circular patch and then far-field radiation pattern will be derived [3].

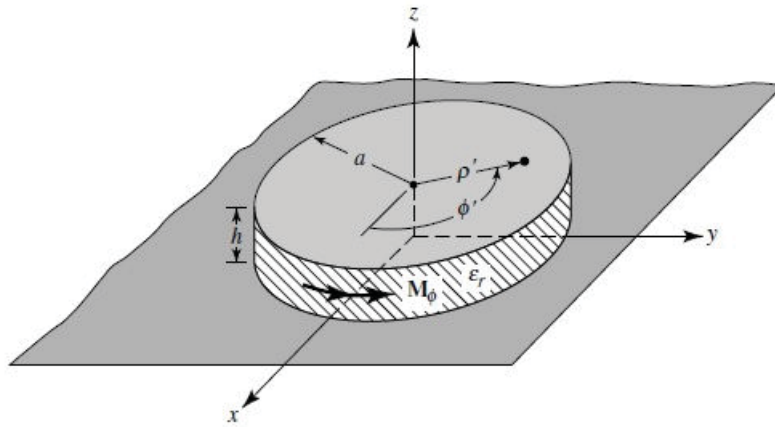


Figure 3.4: Circular patch on an infinite ground plane (taken from [3])

Figure 3.4 shows the model of a circular patch antenna with radius a and substrate thickness of h . The patch is assumed to be a circular cavity with Perfect Electric Conductor (PEC) boundary condition on the top and bottom surfaces of the cavity (representing the patch and ground plane, respectively) and Perfect Magnetic Conductor (PMC) boundary condition on the periphery of the patch.

3.3.1 Cavity Fields

In order to find the fields within the cavity, for the TM^z mode, the following wave equation for the magnetic vector potential is needed to be solved [3]:

$$\nabla^2 A_z(\rho, \phi, z) + k^2 A_z(\rho, \phi, z) = 0 \quad (3.3)$$

Then, the electric and magnetic fields is related to A_z through [3]:

$$E_\rho = -j \frac{1}{\omega \mu \epsilon} \frac{\partial^2 A_z}{\partial \rho \partial z} \quad H_\rho = \frac{1}{\mu} \frac{1}{\rho} \frac{\partial A_z}{\partial \phi} \quad (3.4)$$

$$E_\phi = -j \frac{1}{\omega \mu \epsilon} \frac{1}{\rho} \frac{\partial^2 A_z}{\partial \phi \partial z} \quad H_\phi = -\frac{1}{\mu} \frac{\partial A_z}{\partial \rho} \quad (3.5)$$

$$E_z = -j \frac{1}{\omega \mu \epsilon} \left(\frac{\partial^2}{\partial z^2} + k^2 \right) A_z \quad H_z = 0 \quad (3.6)$$

with the boundary condition of $E_\rho = E_\phi = 0$ on the top and bottom surfaces of the cavity and $H_\phi = 0$ on the periphery of the circular patch. A_z can be written in general as [3]:

$$A_z = B_m n p J_m(k_\rho \rho') [A_2 \cos(m\phi') + B_2 \sin(m\phi')] \cos(k_z z') \quad (3.7)$$

with the constraint of:

$$(k_\rho)^2 + (k_z)^2 = k_r^2 = \omega_r^2 \mu \epsilon \quad (3.8)$$

where $J_m(x)$ is the Bessel function of the first kind and order m , and

$$k_\rho = \chi'_{mn}/a \quad (3.9a)$$

$$k_z = \frac{p\pi}{h} \quad (3.9b)$$

$$m = 0, 1, 2, \dots \quad (3.9c)$$

$$n = 1, 2, 3, \dots \quad (3.9d)$$

$$p = 0, 1, 2, \dots \quad (3.9e)$$

ρ', ϕ' , and z' represent the fields inside the cavity. χ'_{mn} is the n th root of the derivative of $J_m(x)$. The first four values for χ'_{mn} are

$$\chi'_{11} = 1.8412 \quad \chi'_{21} = 3.0542 \quad \chi'_{01} = 3.8318 \quad \chi'_{31} = 4.2012 \quad (3.10)$$

Therefore, according to equation 3.8, the dominant mode for $m, n = 1$ and for $k_z = 0$ or $p = 0$. Thus, the resonance frequency of the dominant mode can be written as [3]:

$$(f_r)_{110} = \frac{1}{2\pi\sqrt{\mu\epsilon}} \left(\frac{\chi'_{11}}{a} \right) = \frac{1.8412c}{2\pi a\sqrt{\epsilon_r}} \quad (3.11)$$

In this analysis, fringing fields have been ignored. To account for these fields, a is needed to be modified to effective radius, a_e , which can be written as [3]:

$$a_e = a \left\{ 1 + \frac{2h}{\pi a \epsilon_r} \left[\ln \frac{\pi a}{2h} + 1.7726 \right] \right\}^{1/2} \quad (3.12)$$

The fields for the dominant mode of the patch can be written as [3]:

$$E_\rho = E_\phi = H_z = 0 \quad (3.13a)$$

$$E_z = E_0 J_1(k\rho') \cos(\phi') \quad (3.13b)$$

$$H_\rho = j \frac{E_0}{\omega \mu_0} \frac{1}{\rho} J_1(k\rho') \sin(\phi') \quad (3.13c)$$

$$H_\phi = j \frac{E_0}{\omega \mu_0} J_1'(k\rho') \cos \phi' \quad (3.13d)$$

where $J_1'(x)$ is the derivative of $J_1(x)$.

3.3.2 Radiated Fields

Equivalence principle can be used to determine the fields radiated by the antenna [6]. Based on this principle, the cavity can be replaced by equivalent electric and magnetic currents. Then, the equivalent current can be plugged into the radiation equations to determine the radiated fields. Cavity is replaced with electric and magnetic surface currents written as [6]:

$$\vec{J}_s = 2\hat{n} \times H_a \quad (3.14a)$$

$$\vec{M}_s = -2\hat{n} \times E_a \quad (3.14b)$$

where \hat{n} is the normal vector on the surface of the cavity. The subscribe a indicates the fields on the surface of the cavity. Since the contribution of magnetic fields to the surface currents is zero at the periphery of the disk (H_ϕ is zero at $\rho' = 0$ and H_ρ is parallel to \hat{n}), and because H_ρ and H_ϕ are negligible on the top and bottom surfaces, the cavity can be replaced with the magnetic current written as [3]:

$$\vec{M}_s = -2\hat{n} \times E_a|_{\rho'=a_e} = \hat{\phi} 2E_0 J_1(ka_e) \cos \phi' \quad (3.15)$$

For far-field radiation, electric and magnetic fields can be written as [6]:

$$E_r \simeq 0 \quad (3.16a)$$

$$E_\theta \simeq -\frac{jk e^{-jkr}}{4\pi r} (L_\phi + \eta N_\theta) \quad (3.16b)$$

$$E_\phi \simeq +\frac{jk e^{-jkr}}{4\pi r} (L_\theta - \eta N_\phi) \quad (3.16c)$$

$$H_r \simeq 0 \quad (3.16d)$$

$$H_\theta \simeq +\frac{jk e^{-jkr}}{4\pi r} \left(N_\phi - \frac{L_\theta}{\eta} \right) \quad (3.16e)$$

$$H_\phi \simeq -\frac{jk e^{-jkr}}{4\pi r} \left(N_\theta + \frac{L_\phi}{\eta} \right) \quad (3.16f)$$

where in cylindrical coordinate system,

$$N_\theta = \iint_S [J_\rho \cos \theta \cos(\phi - \phi') + J_\phi \cos \theta \sin(\phi - \phi') - J_z \sin \theta] e^{jkr' \cos \psi} ds' \quad (3.17a)$$

$$N_\phi = \iint_S [-J_\rho \sin(\phi - \phi') + J_\phi \cos(\phi - \phi')] e^{jkr' \cos \psi} ds' \quad (3.17b)$$

$$L_\theta = \iint_S [M_\rho \cos \theta \cos(\phi - \phi') + M_\phi \cos \theta \sin(\phi - \phi') - M_z \sin \theta] e^{jkr' \cos \psi} ds' \quad (3.17c)$$

$$L_\phi = \iint_S [-M_\rho \sin(\phi - \phi') + M_\phi \cos(\phi - \phi')] e^{jkr' \cos \psi} ds' \quad (3.17d)$$

and

$$r' \cos \psi = \rho' \sin \theta \cos(\phi - \phi') \quad (3.18a)$$

$$ds' = \rho' d\rho' d\phi' \quad (3.18b)$$

For the circular patch antenna with the equivalent currents given by 3.15, $\vec{N} = 0$ and the radiated fields can be written as [3]:

$$E_r = 0 \quad (3.19a)$$

$$E_\theta = -j \frac{ka_e V_0 e^{-jkr}}{2r} [\cos \phi J'_{02}] \quad (3.19b)$$

$$E_\phi = j \frac{ka_e V_0 e^{-jkr}}{2r} [\cos \theta \sin \phi J_{02}] \quad (3.19c)$$

$$J'_{02} = J_0(ka_e \sin \theta) - J_2(ka_e \sin \theta) \quad (3.19d)$$

$$J_{02} = J_0(ka_e \sin \theta) + J_2(ka_e \sin \theta) \quad (3.19e)$$

where $V_0 = hE_0 J_1(ka_e)$. Although the solution ignores the effect of feeds, referring to the Equation 3.14, the fields are derived with the assumption that the patch is excited at $\phi' = 0$. For a patch excited at an arbitrary angle ϕ_0 , the radiated fields can be written as:

$$E_\theta = -j \frac{ka_e V_0 e^{-jkr}}{2r} [\cos(\phi - \phi_0) J'_{02}] \quad (3.20a)$$

$$E_\phi = j \frac{ka_e V_0 e^{-jkr}}{2r} [\cos \theta \sin(\phi - \phi_0) J_{02}] \quad (3.20b)$$

Consequently, for a circular patch excited simultaneously at $\phi_0 = 0$ and $\phi_0 = 90^\circ$ with a phase difference of 90 degrees, the radiated fields may be written as:

$$E_\theta = -j \frac{ka_e V_0 e^{-jkr}}{2r} [J'_{02}(\cos \phi + j \sin \phi)] \quad (3.21a)$$

$$E_\phi = j \frac{ka_e V_0 e^{-jkr}}{2r} [J_{02} \cos \theta (\sin \phi - j \cos \phi)] \quad (3.21b)$$

Equation 3.21 is the final equation for a circular patch antenna excited to generate RHCP wave. These equations can be used in conjunction with Equations 2.6 and 2.7, to evaluate the AR as:

$$AR = \left\{ \frac{X^2 + 1 + \sqrt{X^4 + 1 + 2X^2 \cos(2\Delta\phi)}}{X^2 + 1 - \sqrt{X^4 + 1 + 2X^2 \cos(2\Delta\phi)}} \right\}^{1/2} \quad (3.22)$$

with X defined as:

$$X = \frac{|E_\theta|}{|E_\phi|} = \left| \frac{J'_{02}(\cos \phi + j \sin \phi)}{J_{02} \cos \theta (\sin \phi - j \cos \phi)} \right| = \frac{J'_{02}}{J_{02} \cos \theta} \quad (3.23)$$

and

$$\Delta\phi = \angle E_\theta - \angle E_\phi = -\pi/2 \quad (3.24)$$

thus

$$AR = \left\{ \frac{X^2 + 1 + |X^2 - 1|}{X^2 + 1 - |X^2 - 1|} \right\}^{1/2} \quad (3.25)$$

For an antenna working at $f = 1.57\text{GHz}$ on FR-4 substrate ($\epsilon_r = 4.3$, and using Equation 3.11, the radius of the patch can be found to be $a = 26.4\text{mm}$. Hence, for the given parameters, X is drawn in the Figure 3.5 for θ between 0 and 90 degrees. As shown, X is greater than one for all values of θ . Thus, AR can be written as:

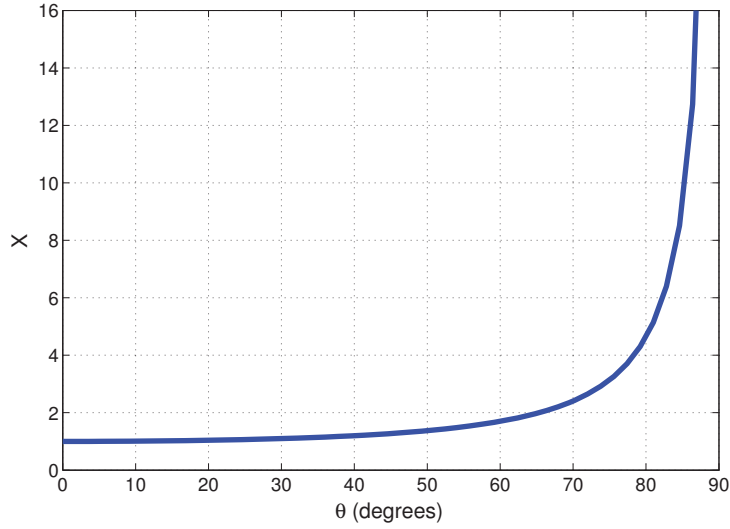


Figure 3.5: Graph of X defined in Equation 3.23

$$AR = X = \frac{J'_{02}}{J_{02} \cos \theta} \quad (3.26)$$

Figure 3.6 demonstrates the evaluated AR. Even for the ideal case of a circular patch, as the graph demonstrates, AR still suffers from the reception of X-polar wave at low angles. AR goes above $2dB$ at $\theta = 45^\circ$ and does not meet the requirement of GPS antenna at angles close to 90 degrees. This behaviour is expected because, as explained in the previous section, the infinite ground plane of the antenna imposes zero electric field for the parallel component of the radiated fields and thus the polarization is linear at $\theta = 90^\circ$.

One important factor in the formula given by Equation 3.26 is the $\cos \theta$ in the denominator. Figure 3.7 represents modified AR given by Equation 3.27 which is the same as the AR defined in Equation 3.26 with the $\cos \theta$ factor removed.

$$AR_{modified} = \frac{J_{02}}{J'_{02}} \quad (3.27)$$

As shown, AR remains below $2dB$ to 90 degrees when this factor is removed. Following the steps given to derive the equation for AR of a circular patch antenna, it can be seen that $\cos \theta$ is an intrinsic factor in fields radiated by a circular patch. This factor is revealed in the equation for E_ϕ (Equation 3.21b). As Equation 3.17 shows, this factor is in the Radiation Equations and is not specifically limited to circular patch antenna. The problem,

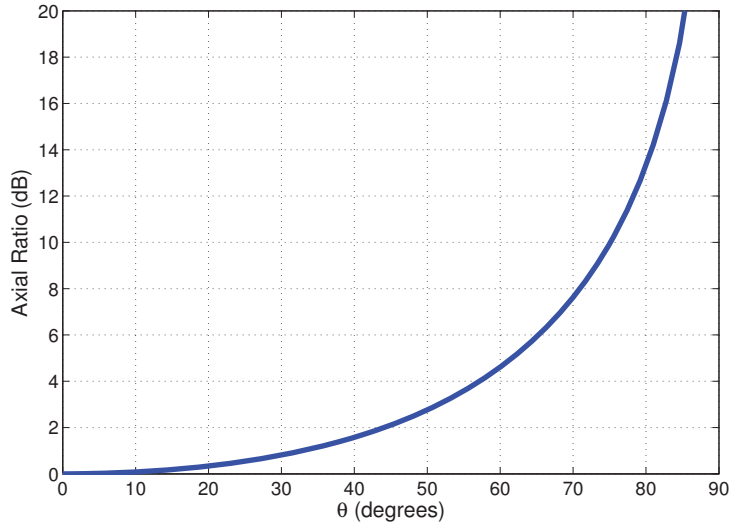


Figure 3.6: Graph of AR (in dB) given in Equation 3.26

however, cannot be solved by simply removing the $\cos \theta$ factor in the E_ϕ component as it is an intrinsic factor in the equations. But the radiated fields of the patch can be modified before entering the far-field region to compensate the $\cos \theta$ factor in the equations.

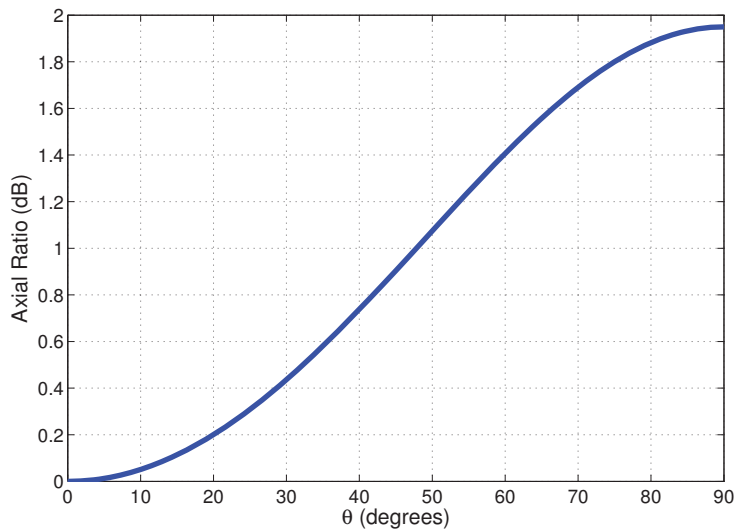


Figure 3.7: Graph of AR (in dB) given in Equation 3.27

The next section discusses the solution presented based on FSS structures.

3.4 Frequency Selective Surface Approach

In this section, an approach will be presented to address the problem raised in the previous section. As discussed, an intrinsic factor of $\cos \theta$ is present in the equation for E_ϕ (3.21b). As it is shown in Equation 3.26, this factor is responsible for the poor AR at low angles. Although this factor may not be removed from the equation for E_ϕ , a similar factor may be added to the E_θ component through implementing an FSS on the top of the antenna.

3.4.1 FSS Design

The purpose of designing the FSS is to place it on the top of the antenna in order to alter the fields radiated by the antenna. The FSS will be designed to add a factor of $\cos \theta$ to the E_θ and leave E_ϕ unchanged. Consequently, the FSS is needed to behave differently with respect to E_θ and E_ϕ as the θ changes. Hence, the goal is to place the FSS in circular arrangement to manipulate E_θ and E_ϕ differently. Our choice of FSS is the non-resonant FSS described by [2] with the non-resonant FSS definition given in Section 1.3.2. As shown in Figure 3.8, the FSS is comprised of two capacitive and one inductive layers. The FSS is required to be transparent at the GPS L1 frequency band. Hence, one resonance frequency with 100MHz of bandwidth would be the desired frequency response of the FSS. A three layer FSS, composed of two capacitive and one inductive layer, provides us with one resonance frequency and the required bandwidth, as will be shown in the next figures.

The goal is to change the FSS parameters for different angles of incidence so that the $\cos \theta$ pattern can be achieved for the magnitude of E_θ . The FSS shown in Figure 3.8 can be modeled by the lumped element network shown in Figure 3.9 with the capacitive patches replaced by a capacitor and inductive layers modeled by an inductor. The substrates can be modeled by transmission lines. Since the thicknesses of the substrates are much smaller than the wavelength, the transmission line models can be replaced with their lumped element network as shown in Figure 3.9b [2].

For the capacitive patches inside the medium with relative permittivity of ϵ_r , equivalent network elements for the two TE and TM polarizations can be written as [35]:

$$C_{TM} = \frac{2\epsilon_r\epsilon_0}{\pi} \ln \left(\frac{1}{\sin \frac{\pi t_1}{2W}} \right) \quad (3.28a)$$

$$C_{TE} = \frac{2\epsilon_r\epsilon_0}{\pi} \ln \left(\frac{1}{\sin \frac{\pi t_1}{2W}} \right) \left(1 - \frac{k_0^2}{k_{eff}^2} \sin^2 \theta \right) \quad (3.28b)$$

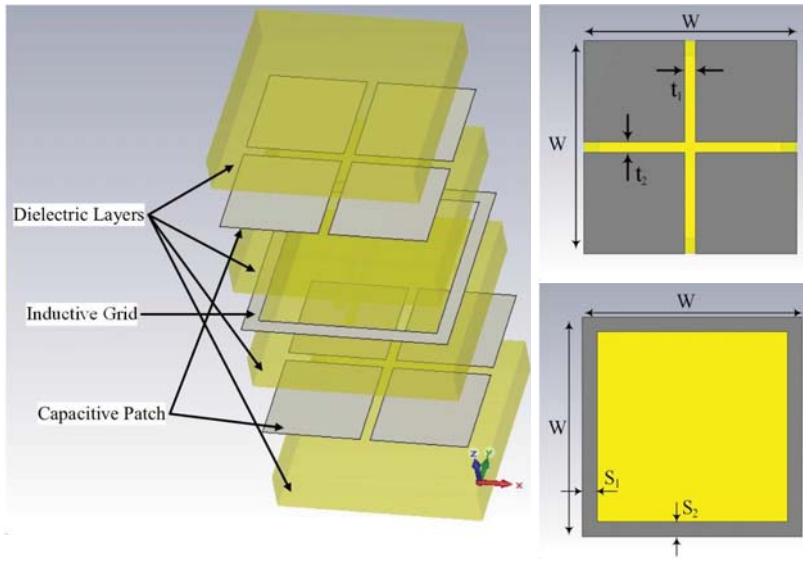


Figure 3.8: FSS unit cell structure

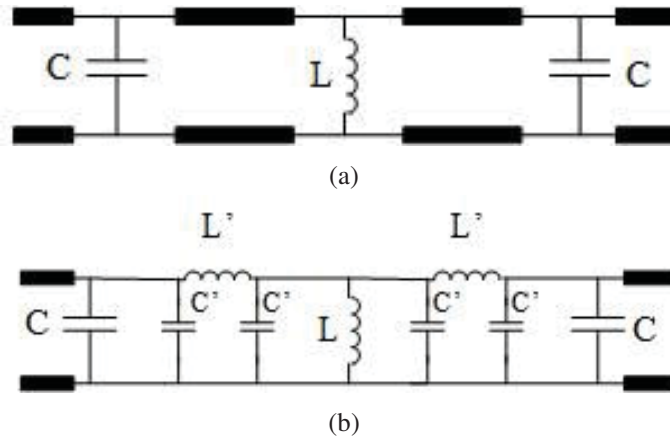


Figure 3.9: Equivalent network of the non-resonant FSS (a) dielectric layers modeled by transmission lines (b) transmission lines replaced by lumped element equivalents.

And for the inductive grids, the equivalent inductance can be written as [35]:

$$L_{TM} = \frac{\mu_0 W}{2\pi} \ln \left(\frac{1}{\sin \frac{\pi s_1}{2W}} \right) \left(1 - \frac{k_0^2}{k_{eff}^2} \frac{\sin^2 \theta}{2} \right) \quad (3.29a)$$

$$L_{TE} = \frac{\mu_0 W}{\pi} \ln \left(\frac{1}{\sin \frac{\pi s_2}{2W}} \right) \quad (3.29b)$$

With the parameters defined in Figure 3.8. k_0 is the free space wave number and k_{eff} is the wave number in the dielectric region. L' and C' can be written as ([2]) $L' = \mu_0 h$

and $C' = \epsilon_0 \epsilon_r h / 2$, respectively. For the equations given for network elements, and using Equations 2.3 and 2.5, S -parameters of the equivalent network can be derived. Since the FSS is required to be transparent at $f = 1.575\text{GHz}$ only, with no strict limitation on the bandwidth, the parameters of the FSS can be found to have the resonance frequency at $f = 1.575\text{GHz}$. The substrates are Taconic RF-43 materials ($\epsilon_r = 4.3$) with the standard thickness of 1.57mm . Hence, with the equations given for the capacitance and inductance of the FSS, and similar to the Section 2.1.1, transmission properties of the FSS can be derived. Analytical model can be used to find the closest design parameters. Then tuning is performed to obtain the best parameters for the desired behaviour of the FSS. Figure 3.10 compares the S -parameters of the FSS using analytical model and also using simulations with the geometrical parameters given in Table 3.1. The model is simple and does not take into account the effect of mutual coupling between the layers. A series capacitor can be included in the model between each two adjacent layers to account for the mutual coupling of the layers. Moreover, for the sake of simplicity, capacitance of inductive layers and also inductance of capacitive layers have been ignored. There is good agreement between the analytical and simulation results with the considerations given above. The FSS has been simulated using CST Microwave Studio.

Parameter	W	t_1	t_2	s_1	s_2
Value	15.7mm	1mm	1mm	1.52mm	1.52mm

Table 3.1: Physical properties of non-resonant FSS unit cell

The size of the unit cell is chosen so that to have as many number of unit cells as possible on the antenna while keeping other parameters of the FSS reasonable. Parameters given in Table 3.1 are to demonstrate the behaviour of the FSS versus frequency. In the next subsection, design procedure of the FSS will be described to obtain the aforementioned behaviors for E_θ and E_ϕ .

3.4.2 Tapering procedure of the FSS

As discussed earlier, since the antenna has circular symmetry, the FSS will be distributed in circular arrangement on the top of the antenna, as shown in Figure 3.11.

Since the FSS is in close proximity of the antenna, an appropriate analytical model of the Circularly Arranged FSS (CAFSS) for the incident waves of the antenna is a pretty

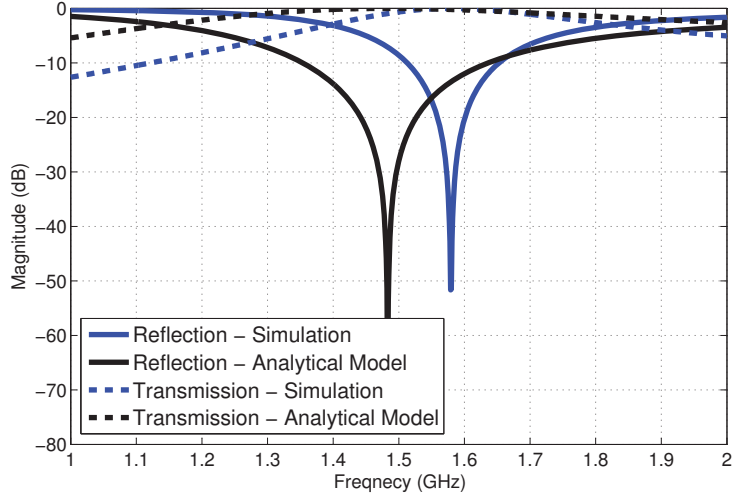


Figure 3.10: Comparison between the simulation and analytical model of FSS transmission properties for normal incidence.

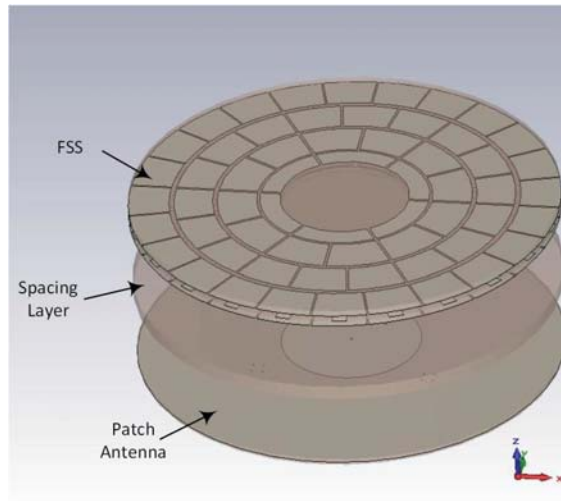


Figure 3.11: Expanded view of the FSS in circular arrangement on the antenna.

tough to obtain. On the other hand, parameters of CAFSS cannot be obtained using software simulation because the boundary condition of the each unit cell does not maintain as we move from one circle to another and Rectangularly Arranged FSS (RAFSS) can only be simulated in the unit cell simulation of the software. Since the FSS is circularly distributed, the TE and TM plane wave incidence polarizations in the unit cell simulation of FSS (rectangular coordinates) correspond to the E_ϕ and E_θ of CAFSS, respectively (see Figure 3.12).

Hence, the following procedure will be pursued to find the appropriate parameters of the CAFSS.

- Derive the RAFSS parameters for different angles of incidence to obtain the $\cos \theta$ and unity transmission coefficients for TM and TE polarizations, respectively.
- Use the derived RAFSS parameters for CAFSS for each row of unit cells corresponding to its closest angle of incidence. (Assuming that the wave is emanating from the edge of the patch antenna and then reaching the FSS.)
- Extract the far-field results of the structure.
- Tune the CAFSS parameters.
- Repeat the last two steps to obtain the desired $\cos \theta$ pattern for the E_θ component.

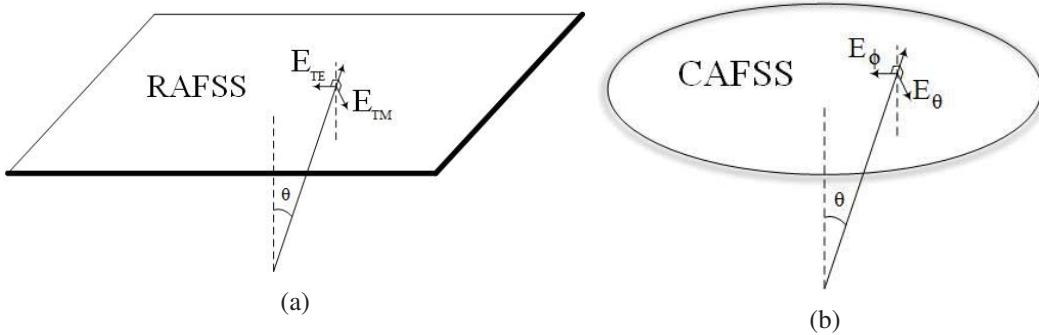


Figure 3.12: Electric fields incident on the FSS (a) on RAFSS (b) on CAFSS

Table 3.2 demonstrates the parameters of the RAFSS for different angles of incidence. Parameters are chosen so that the FSS exhibit transmission coefficient of $\cos \theta$ and unity for TM and TE modes, respectively. T_{TM} and T_{TE} are the transmission coefficients for the TM and TE polarized electric fields, respectively. The parameters not mentioned in this table are the same as those presented in Table 3.1. The subscribes 1 and 2 refer to TE and TM modes, respectively.

In the next section, the RAFSS will be implemented in CAFSS form on top of the antenna and then the parameters will be tuned to achieve the required pattern of E_θ and E_ϕ versus θ .

Angle of Incidence	$t_1(mm)$	$t_2(mm)$	$s_1(mm)$	$s_2(mm)$	$\cos \theta$	T_{TM}	T_{TE}
$\theta = 0^\circ$	1	1	1.52	1.52	1	1	1
$\theta = 10^\circ$	1	1	1.52	1.6	0.98	0.94	0.96
$\theta = 20^\circ$	0.95	1.1	1.52	1.6	0.93	0.89	0.97
$\theta = 30^\circ$	0.95	1.1	1.4	1.8	0.86	0.77	0.98
$\theta = 40^\circ$	0.9	1.1	1.3	2	0.76	0.71	1
$\theta = 50^\circ$	0.9	1.3	1.3	2.3	0.64	0.57	0.97
$\theta = 60^\circ$	0.85	1.4	1.3	2.9	0.5	0.47	0.91
$\theta = 70^\circ$	0.8	2	1	4	0.34	0.36	0.99
$\theta = 80^\circ$	0.5	3.5	0.65	7.8	0.173	0.18	0.99

Table 3.2: Physical properties of non-resonant FSS unit cell

3.5 CAFSS on Top of The Antenna

In this part, the FSS presented in the previous part will be implemented in circular arrangement represented as CAFSS. Since there is restrictions on the overall size of the antenna, only limited number of unit cells will be implemented on the structure. Although the FSS is simulated with the assumption that there are infinite number of unit cells present, it will be shown that a few rows of unit cells provide the required behavior for the incident wave of the patch antenna.

3.5.1 Implementation

Figure 3.13 shows the view of the FSS distributed in circular shape. Figures 3.13a and 3.13b show the capacitive and inductive layers, respectively. The goal is to maintain the periodicity of the FSS along the ϕ and r directions. Thus, the number of cells increases as we move from inner to outer rows.

Figure 3.14 shows the side view of the CAFSS and antenna. r_i is the distance of the i th row of FSS from the center. W_r is the width of each row of FSS and h_f is the spacing between the antenna and the FSS. The goal to evaluate closest θ_i for each row of the FSS.

Thus, assuming that the fields are emanating from the edge of the patch antenna, θ_i can be found as follows:

$$\theta_i = \tan^{-1} \left(\frac{r_i - R_p}{h_f} \right) \quad (3.30)$$

and r_i can be written as:

$$r_i = W_r i \quad (3.31)$$

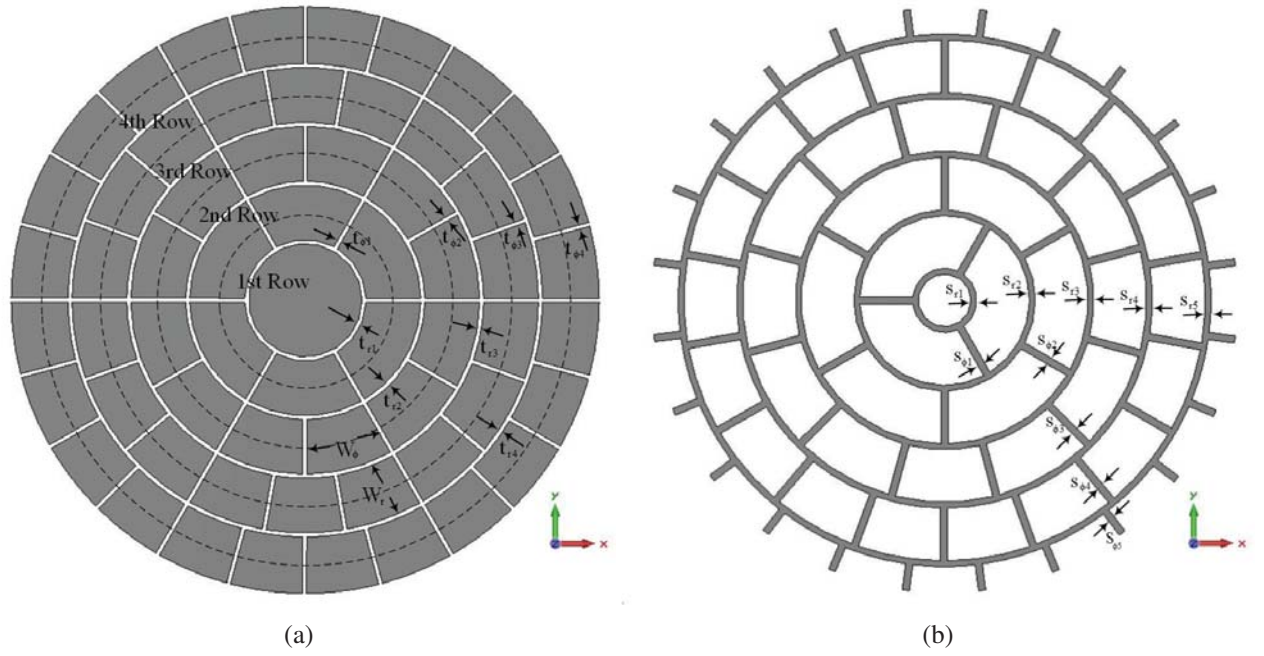


Figure 3.13: Geometry of CAFSS (a) Capacitive layer (b) Inductive layer.

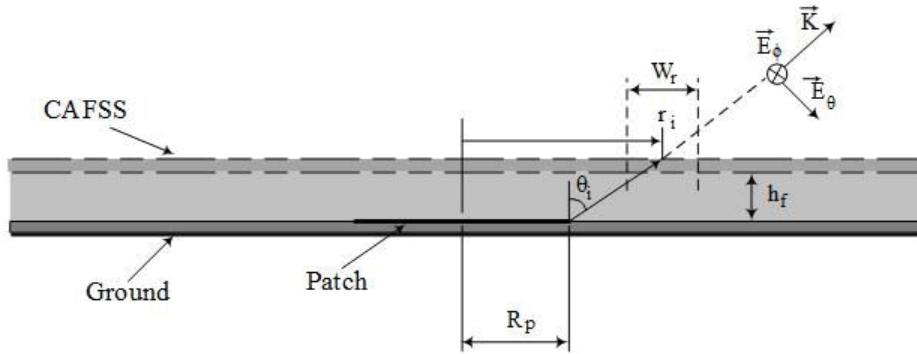


Figure 3.14: Side view schematic of the CAFSS on the antenna.

Hence,

$$\theta_i = \tan^{-1} \left(\frac{W_r i - R_p}{h_f} \right) \quad (3.32)$$

In order to maintain the phase of the wave in all of the directions, the spacing between the antenna and the FSS is required to be filled with the same material as the antenna substrate and FSS. A greater spacing results in a better performance since θ_i does not greatly change from one row of FSS to another. A large h_f , however, increases the size of the antenna which is undesirable for many applications. Hence, h_f is needed to be kept as small as possible while the required performance of the FSS can be achieved. For our case, with the RF-43

material, h_f is chosen to be 6.35mm. As stated earlier, our choice of W_r is 15mm. Given these parameters, θ_i for each row of FSS can be found as:

$$\theta_1 = -55.38^\circ \quad (3.33a)$$

$$\theta_2 = 42.4^\circ \quad (3.33b)$$

$$\theta_3 = 73.02^\circ \quad (3.33c)$$

$$\theta_4 = 79.94^\circ \quad (3.33d)$$

$$\theta_5 = 82.87^\circ \quad (3.33e)$$

For the values θ_i given in Equation 3.33, and using values of Table 3.2, required parameters of the CAFSS can be derived. Table 3.3 shows these parameters with the parameters defined in Figure 3.13.

Row Number	$i = 1$	$i = 2$	$i = 3$	$i = 4$	$i = 5$
$t_{ri}(mm)$	1.35	1.3	2.5	3	3.2
$t_{\phi i}(mm)$	0.76	0.84	0.68	0.55	0.54
$s_{ri}(mm)$	1.3	1.3	0.95	0.65	0.6
$s_{\phi i}(mm)$	2.45	1.85	5	7.8	8

Table 3.3: Parameters of CAFSS

The parameters of the first row of FSS is greatly different from the other rows and does not satisfy the boundary condition of unit cell as it is at the middle of the FSS. Moreover, the first row has a great effect on the properties of the patch antenna and affect the radiation properties of the antenna. Thus, the antenna and the FSS will exhibit a better performance when the first row of the FSS is removed in terms of the input impedance and also the AR. Figure 3.15 shows the structure of the antenna and CAFSS with and without the first row of the CAFSS. The parameters are those given in Table 3.3.

Figure 3.16 shows the simulation result of AR for the structure at four different planes. As shown, AR is improved compared to the antenna with the infinite ground plane. However, AR still is needed to be improved to satisfy the requirement of the GPS system. Figure 3.17 demonstrates $|E_\theta|/|E_\phi|$ for different angles. The best AR is achieved when this ratio approaches unity because the phase difference of the E_θ and E_ϕ remains relatively constant

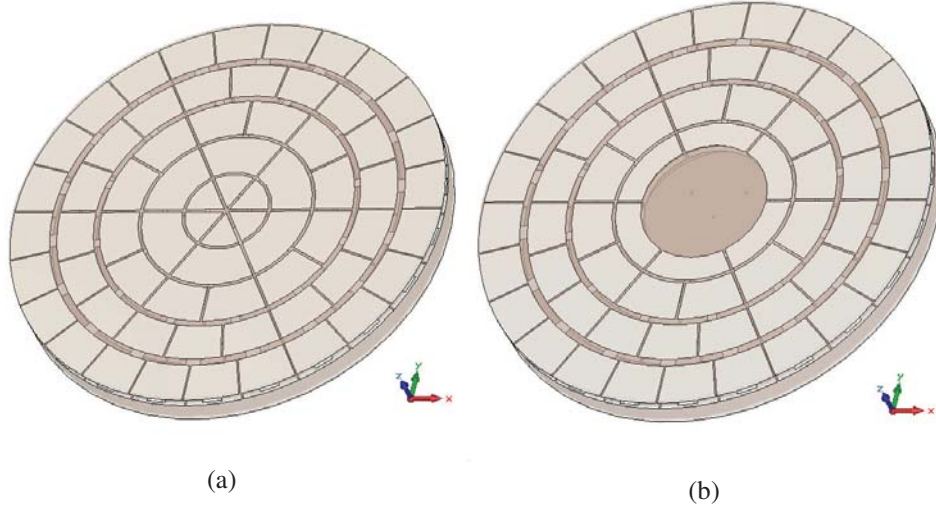


Figure 3.15: Simulation view of the structure with the parameters given in Table 3.3 (a) complete CAFSS (b) first row of CAFSS removed .

about $\pi/2$ over different angles. In the next step, the parameters of the CAFSS will be tuned to improve the $|E_\theta|/|E_\phi|$ ratio and hence improve the AR at all of the angles.

The next sub-section discusses the final parameters of the structure along with the simulation results.

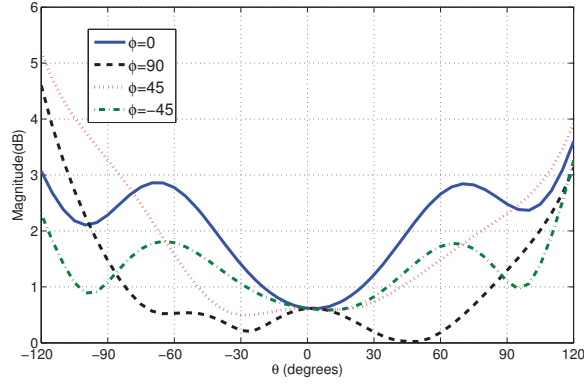
3.5.2 Simulation Results

Table 3.4 shows the final parameters of the CAFSS starting from the second row. The parameters are adjusted for the best AR at all of the planes.

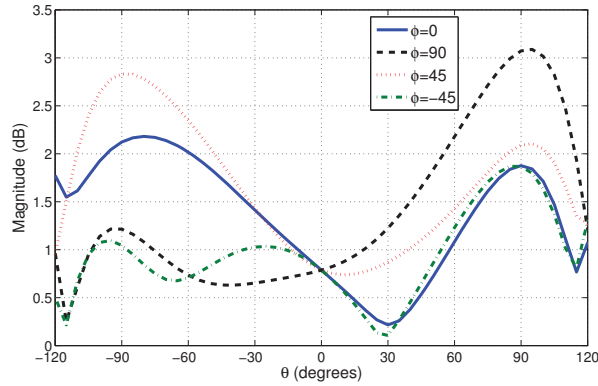
Row Number	$i = 2$	$i = 3$	$i = 4$	$i = 5$
$t_{ri}(mm)$	1	2	2.2	3
$t_{\phi i}(mm)$	1	1	0.85	0.65
$s_{ri}(mm)$	1.5	1.45	1.35	1.2
$s_{\phi i}(mm)$	2	2.9	4	7.8

Table 3.4: Final parameters of CAFSS

To generate the CP wave, the patch antenna is excited at two points 45° apart with 90° phase difference. A 90° hybrid phase shifter and power divider in circular shape is used to excite the patch antenna and generate CP wave. Design procedure of the 90° hybrid network as well as the simulation results will be discussed in the next section.



(a)

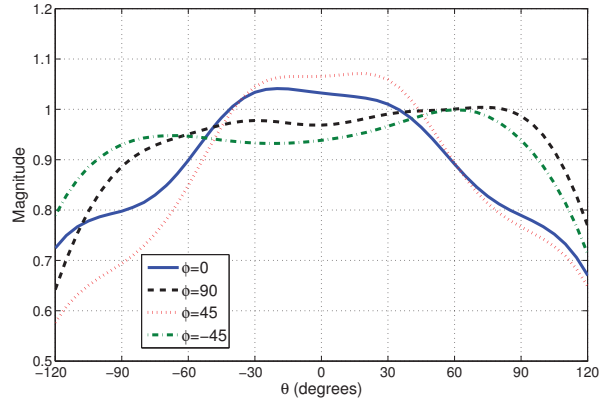


(b)

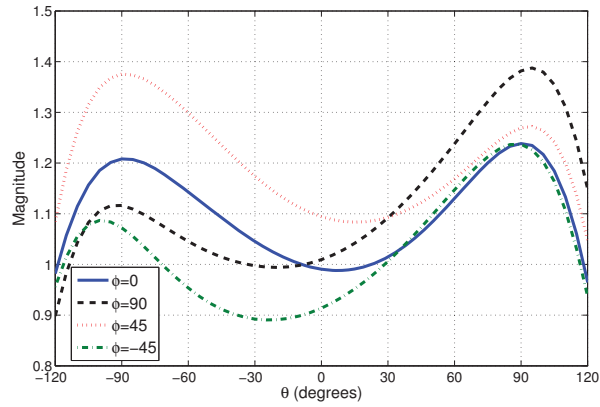
Figure 3.16: AR of the structures shown in Figure 3.15 with the tapering parameters given in Table 3.3(a) complete CAFSS (b) first row of CAFSS removed .

Figure 3.18 shows the simulation result of the radiation pattern of the patch antenna with CAFSS, for the parameters given in Table 3.4. AR at different planes are shown in Figure 3.19. As shown, the final structure exhibits AR of better than $2dB$ at angles up to 100° . Figure 3.20 shows the ratio of $|E_\theta|/|E_\phi|$ at different angles. The ratio remains relatively constant about unity. Figure 3.21 shows the proximity of the profile of $\cos \theta$ function to the analytical $\cos \theta$ function. Referring to Equations 3.26 and 3.27 for AR and $AR_{modified}$, the profile is calculated by dividing AR of the final structure with the CAFSS by the AR of the antenna alone without any FSS, on the infinite ground plane. Although there are many simplifications considered in evaluating the profile, there is still good match with the analytical $\cos \theta$ function.

AR and radiation pattern evidently express the effect of the CAFSS on the improvement



(a)



(b)

Figure 3.17: Ratio of $|E_\theta|/|E_\phi|$ of the structures shown in Figure 3.15 with the tapering parameters given in Table 3.3.

of the AR of the patch antenna at the angles close to 90° .

Figures 3.22 and 3.23 show the simulation results for the gain and radiation efficiency of the antenna for the two cases of the antenna alone and also antenna combined with the CAFSS. Evidently, combining the antenna with CAFSS has resulted in the increase of the gain of the antenna. This can be due to the fact that the physical aperture of the antenna has been increased by putting the CAFSS on the antenna. Therefore, the increase in the gain of the antenna may be expected.

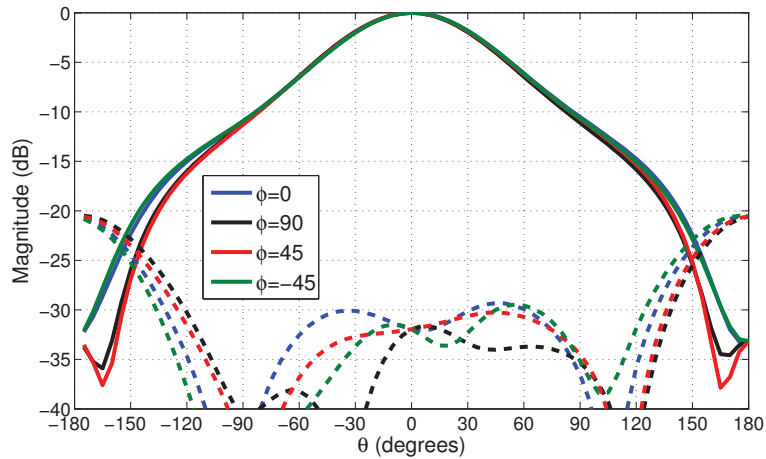


Figure 3.18: Simulated radiation pattern of the antenna with CAFSS combined with the power divider. Solid lines and dashed lines represent RHCP and LHCP waves, respectively.

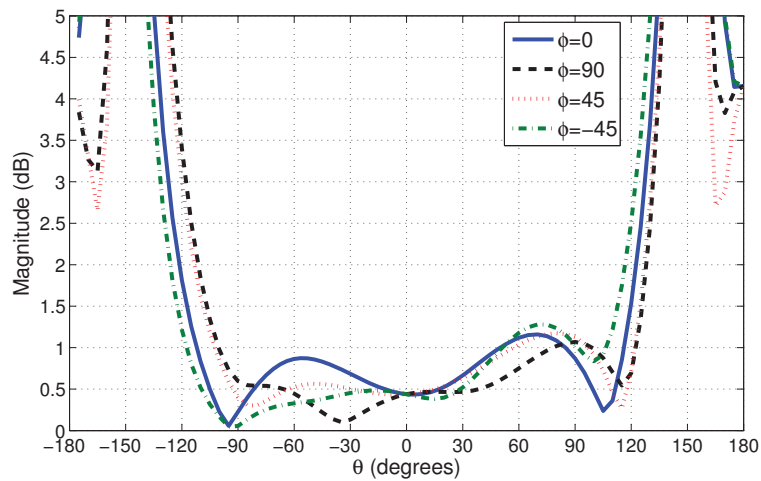


Figure 3.19: Simulated AR of the final structure with the parameters given in Table 3.4.

3.6 Other Measures of the Antenna

Beside the parameters discussed and evaluated in previous sections, there are other parameters defined for the GPS antenna which describe the sufficiency of the antenna signal reception. These parameters are Phase Center (PC) and Up/Down Ratio (UDR) and are conventionally used to assess the performance of the antenna.

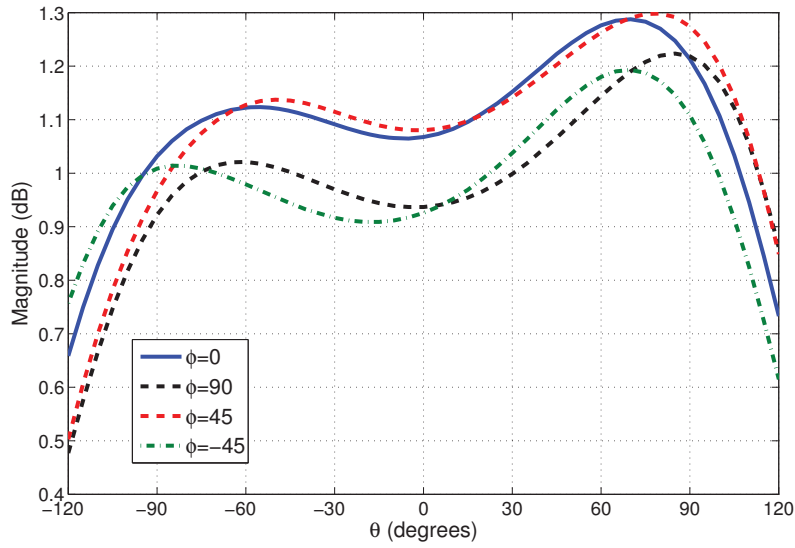


Figure 3.20: Ratio of $|E_\theta|/|E_\phi|$ of the final structure with the parameters given in Table 3.4.

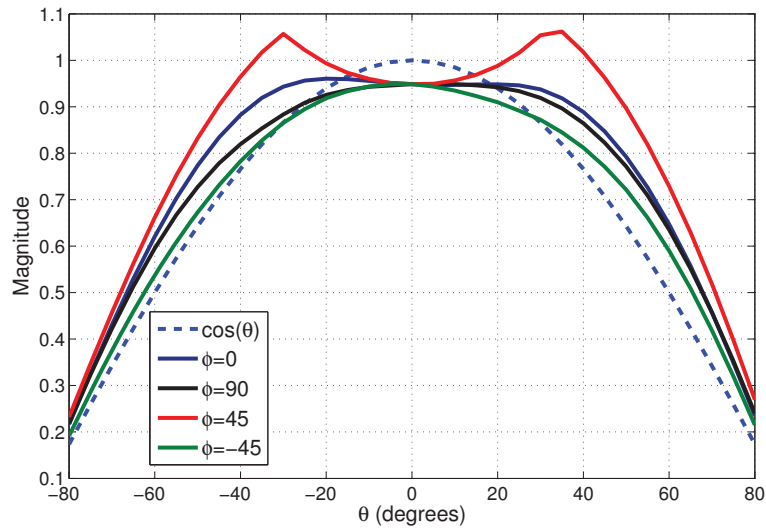


Figure 3.21: $\cos \theta$ profile achieved for the CAFSS used. Dashed line is the $\cos \theta$ function and solid lines are the profiles found by the radiated fields of the antenna at different angles.

3.6.1 Phase Center

Referring to [36], phase center is defined as "The location of a point associated with an antenna such that, if it is taken as the center of a sphere whose radius extends into the far-field,

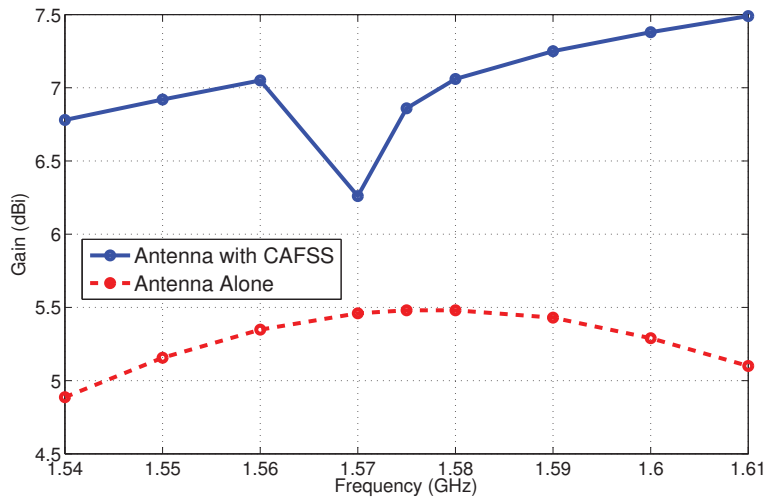


Figure 3.22: Simulation results for the gain of the antenna versus frequency. Solid and dashed lines are the results for the antenna with CAFSS and antenna alone, respectively.

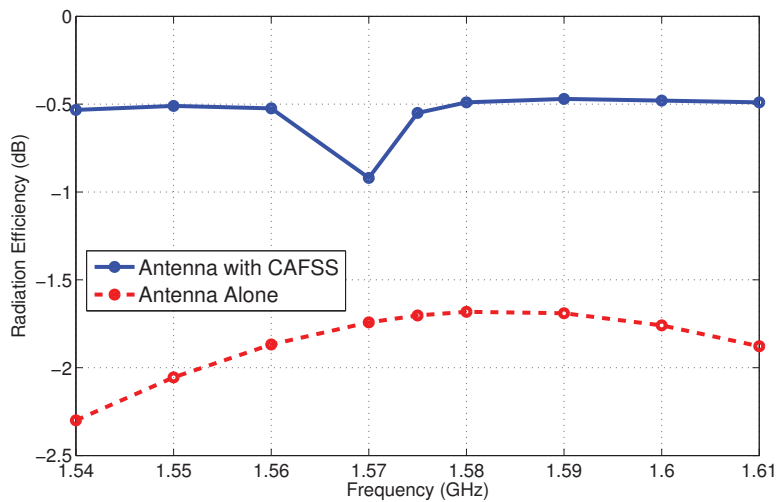


Figure 3.23: Simulation results for the radiation efficiency of the antenna versus frequency. Solid and dashed lines are the results for the antenna with CAFSS and antenna alone, respectively.

the phase of a given field component over the surface of the radiation sphere is essentially constant, at least over that portion of the surface where the radiation is significant.”. Based on this definition, the PC location of the GPS antenna is required to remain constant over the bandwidth as it is the indication of the actual place of the antenna and measurements of the location of the receiving antenna are based on the phase center location. Figure 3.24

shows the location of PC over the bandwidth. As demonstrated, PC movements are on the order of few millimeters which is below the requirement of the GPS system.

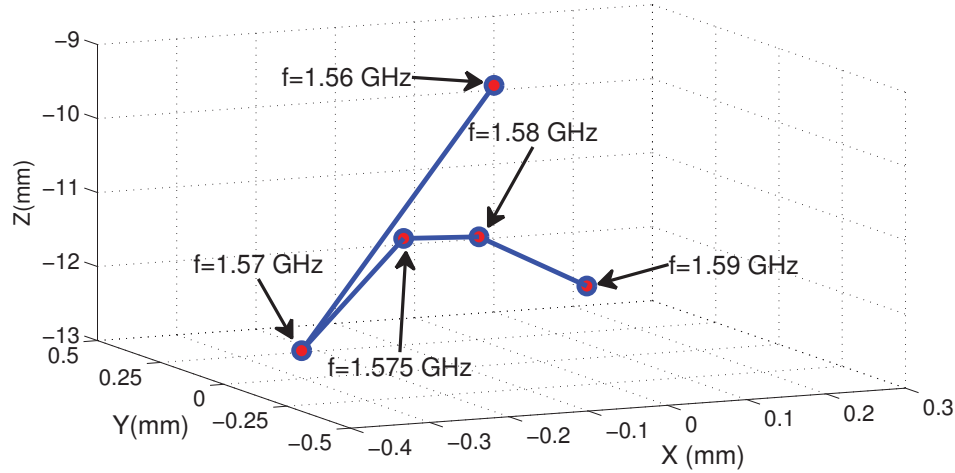


Figure 3.24: Phase center displacement of the antenna versus frequency.

3.6.2 Up/Down Ratio

Up/Down Ratio (UDR) is defined as the ratio of the RHCP gain of the antenna and upper hemisphere at the angle θ divided by the LHCP gain of the antenna at the same angle at the lower hemisphere [7]. It can be written as [22](See Figure 3.25) :

$$UDR = \frac{G_{RHCP}(\theta)}{G_{LHCP}(\pi - \theta)} \quad (3.34)$$

Using this definition, the ratio is evaluated and shown in Figure 3.26 for different planes. As shown, the antenna exhibits a UDR of better than 20dB at all of the angles.

3.7 Effect of the Size of CAFSS

As indicated in Figure 3.15, the CAFSS discussed in this chapter contains three and a half of rows of CAFSS. However the design procedure discussed in this chapter is not limited to this number of rows for the CAFSS and the procedure can be simply assigned to larger CAFSSs. In this section, the number of rows of CAFSS is increased by one and the design parameters are derived for the larger CAFSS. Since the structure with smaller profile is

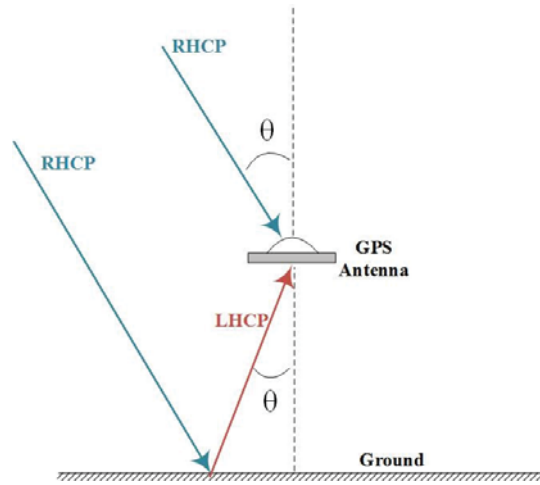


Figure 3.25: Multipath with the reflection occurring at the ground.

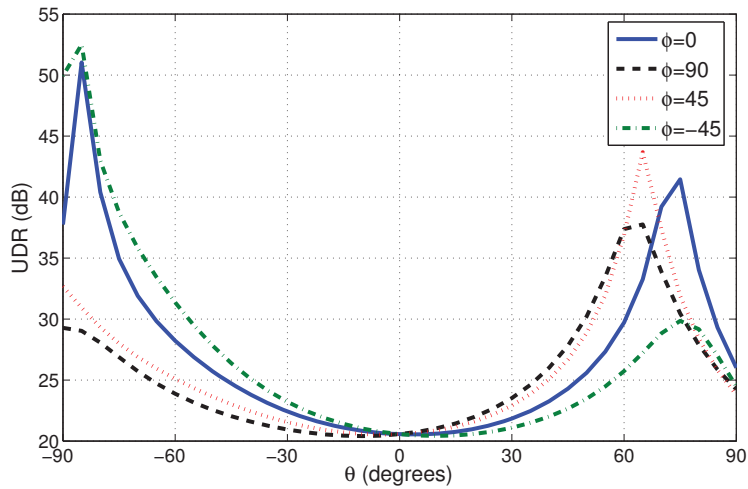


Figure 3.26: Up/Down Ratio (UDR) of the antenna evaluated at different angles.

desirable and all the required features are derived for the antenna, the CAFSS designed in previous sections is considered as the final structure and the larger CAFSS is only evaluated for the sake of parametric study.

The structure shown in Figure 3.27, shows the view of CAFSS with the number of rows increased by one. The required parameters of the CAFSS can be found using Equation 3.32. These parameters may be used as the starting point to find the best values for CAFSS, as stated earlier. Table 3.5 shows the final parameters of CAFSS after tuning the parameters of the CAFSS for the best axial ratio.

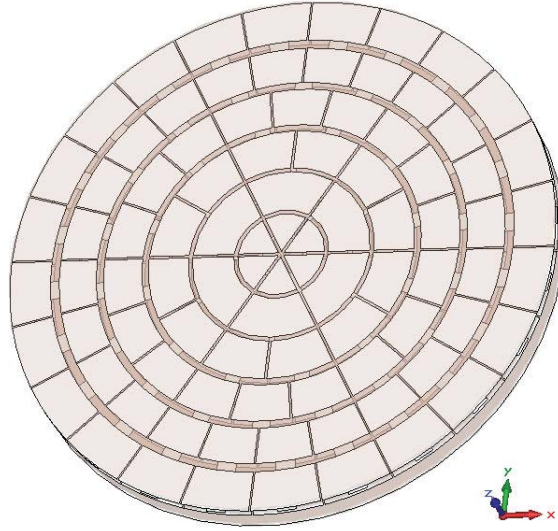


Figure 3.27: View of the structure with the increased number of rows of CAFSS.

Row Number	$i = 1$	$i = 2$	$i = 3$	$i = 4$	$i = 5$	$i = 6$
$t_{ri}(mm)$	1.35	1.3	2.13	2.4	2.9	2.9
$t_{\phi i}(mm)$	1	0.84	0.84	0.68	0.55	0.55
$s_{ri}(mm)$	1.3	1.3	0.95	0.65	0.6	0.6
$s_{\phi i}(mm)$	1.3	1.85	5	5.77	6.3	6.3

Table 3.5: Parameters of CAFSS

The biggest changes are to the last row of CAFSS since there is an obvious change to the periodic boundary condition for this row. Simulation results for the structure and the parameters given is shown in Figures 3.28 and 3.29 for the axial ratio and the radiation pattern of the antenna, respectively. Axial ratio of better than 2.1dB is achieved at angles up to 140 degrees at all of the planes. The gain of the antenna is 6.9dB and the diameter of the structure is 18cm ($\sim \lambda$). The number of rows for the CAFSS can still be increased further. However, we stop at this step and leave a more comprehensive study on the size of CAFSS to future as all of the requirements demanded are attained by the CAFSS with 3.5 rows.

For a smaller CAFSS, with less number of unit cells, a desirable response cannot be achieved both in terms of input impedance and radiation pattern. It can be due to the fact

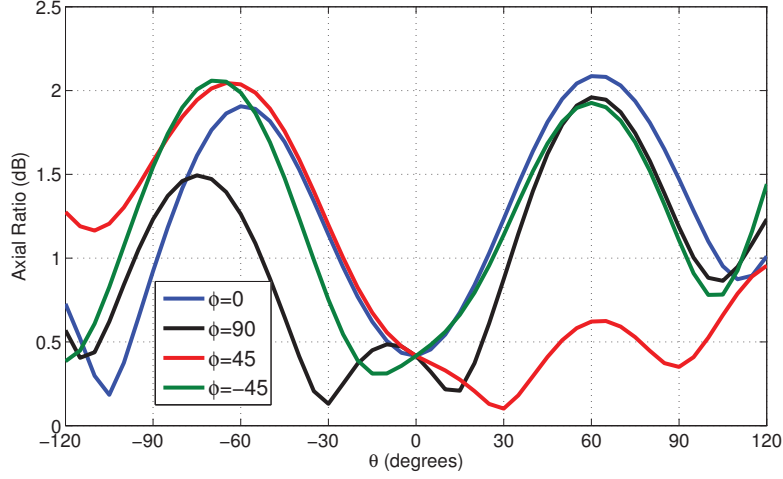


Figure 3.28: Simulation result for the axial ratio of the structure with increased number of rows in CAFSS.

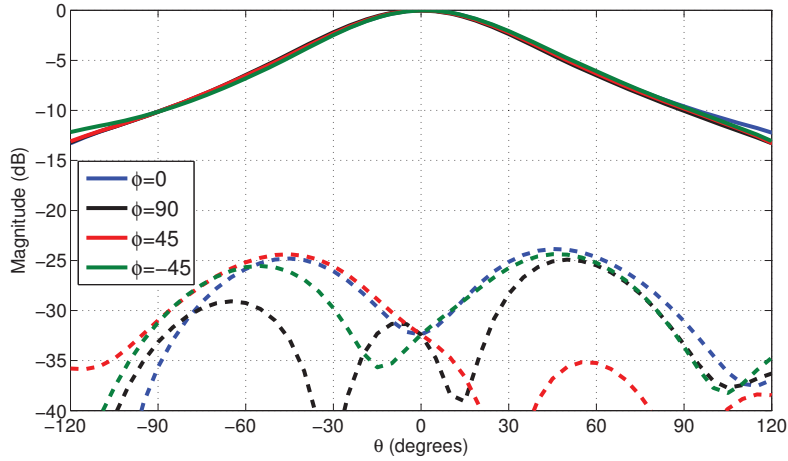


Figure 3.29: Simulation results for the radiation pattern of the structure with increased number of rows in CAFSS.

that the FSS is a periodic structure and hence in order to draw the desired behaviour from the FSS, there must be enough number of unit cells. For the CAFSS with less number of unit cells, the FSS hardly act as a transparent superstrate at the desired frequency and thus affect the radiation pattern features as well as the input impedance of the antenna.

3.8 Effect of Proximity to the Ground

Since the GPS antenna is usually mounted on grounded based stations, it is covered by the ground on one side. Thus, it is important to evaluate the effect of proximity to the ground in order to make sure that the antenna provides the required performance under common terrestrial circumstances.

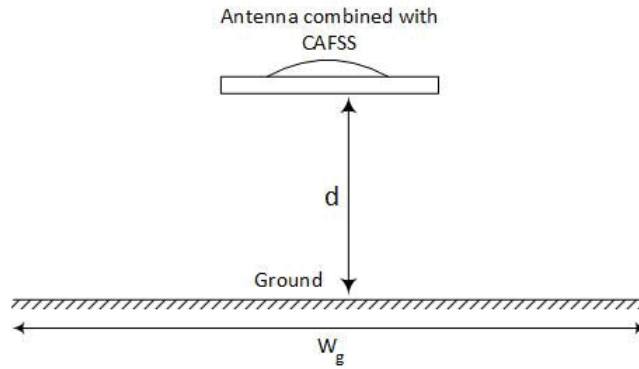


Figure 3.30: Simulation results for the radiation pattern of the structure with increased number of rows in CAFSS.

A ground plane with the size of $2\lambda \times 2\lambda$ is placed on the ground plane side of the antenna at a distance d from the antenna (see Figure 3.30). Figure 3.31 shows the axial ratio of the antenna for different distances from the ground, at four different planes ($\phi = 0, 90, 45, -45$). As shown, for distances larger than 2λ ($\sim 40cm$), the axial ratio of the antenna can be guaranteed to maintain its regular behaviour as there is no ground on one side of the antenna.

Figure 3.32 demonstrates the effect of increasing the ground plane size for different ground sizes, $W_g = 2\lambda, 3\lambda$, and 4λ (see Figure 3.30). As shown, increasing the size of the ground plane, while keeping its distance constant from the antenna, can still affect the performance of the antenna.

In conclusion, since the axial ratio of the antenna is a sensitive parameter, appropriate considerations are needed to be taken into account when designing and mounting the antenna on any plant.

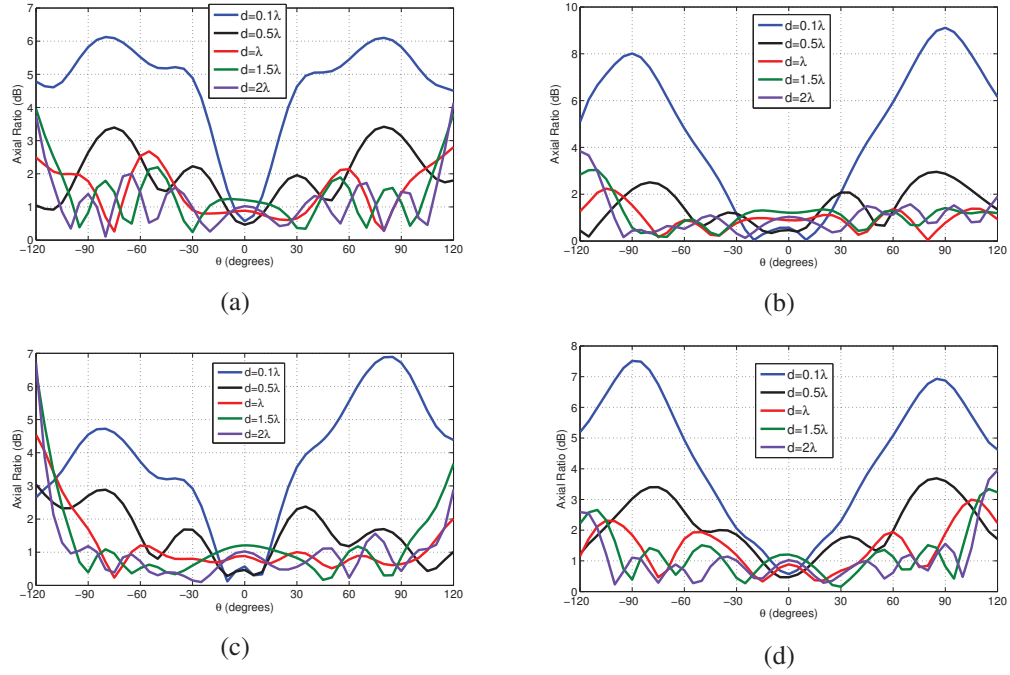


Figure 3.31: Axial ratio of the antenna for different distances from the ground with the size of $2\lambda \times 2\lambda$ (a) $\phi = 0^\circ$ (b) $\phi = 45^\circ$ (c) $\phi = 90^\circ$ (d) $\phi = -45^\circ$

3.9 90° Hybrid Phase Shifter

Figure 3.33 shows the schematic of a 90° hybrid. S -parameters matrix of the the network can be written as [4]:

$$[S] = \frac{1}{\sqrt{2}} \begin{bmatrix} 0 & j & 1 & 0 \\ j & 0 & 0 & 1 \\ 1 & 0 & 0 & j \\ 0 & 1 & j & 0 \end{bmatrix} \quad (3.35)$$

As the S -parameters matrix of the network shows, when excited at port 1, the power divides between ports 2 and 3 with a phase difference of 90° and no power couples into port 4. Ports are connected through four branches of quarter wavelength transmission lines with characteristic impedances of Z_0 and $Z_0/\sqrt{2}$ where Z_0 is the characteristic impedance of the system where all the ports have to be matched to. Basics of the design are discussed in details in [4].

For our application, we require the 90° hybrid be adequately adjusted for the circular shape of the structure. Hence, the power divider is designed in circular shape (similar to the one

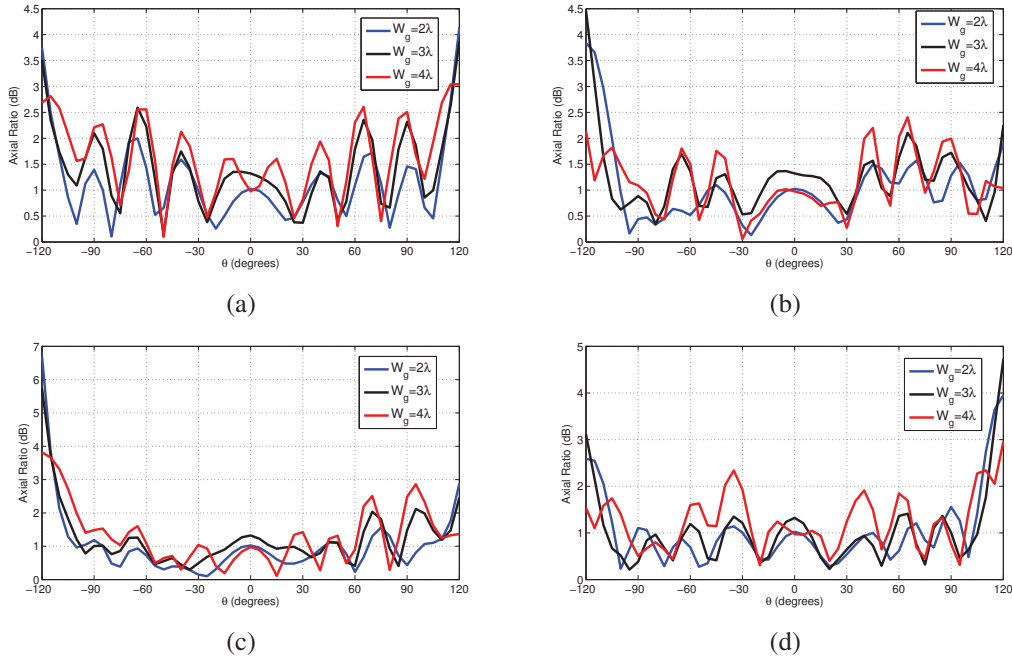


Figure 3.32: Axial ratio of the antenna for different ground sizes at the distance 2λ away from the antenna (a) $W_g = 2\lambda$ (b) $W_g = 3\lambda$ (c) $W_g = 4\lambda$

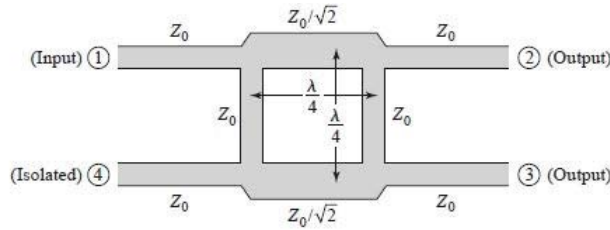


Figure 3.33: Schematic of 90° hybrid (taken from [4]).

presented in [22]). The network is shown in Figure 3.34. The circle of the network is comprised of four quarter-wavelength microstrip lines placed consecutively with characteristic impedances of Z_0 and $Z_0/\sqrt{2}$. Thus, the circle has the perimeter of one wavelength. For the substrate with the relative permittivity of 4.3 and thickness of 0.79mm , the effective permittivity can be found to be 3.27. Thus the effective wavelength for the transmission line (λ_{eff}) is 10.57cm and R_h , radius of the 90° hybrid, is 16.8mm . The structure will be designed for 50Ω system. Therefore, W_1 and W_2 can be found to be 1.54mm and 2.63mm , respectively. Simulation results for the S -parameters of the 90° hybrid is shown in Figure 3.35. Figure 3.36 shows the transmission phase difference for ports 2 and 3.

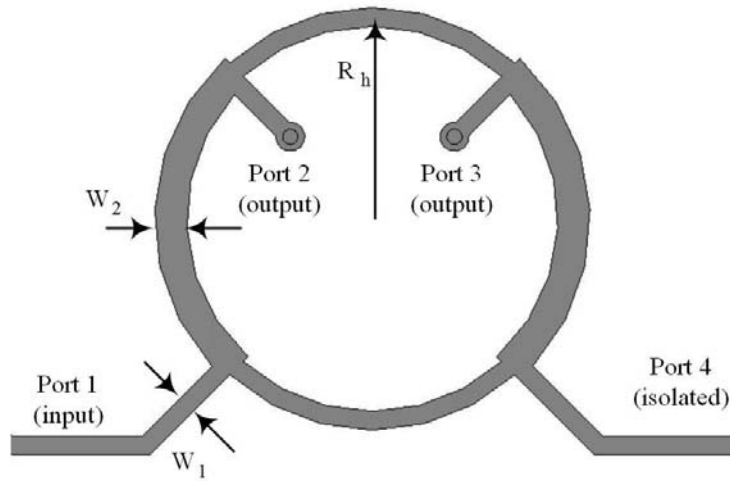


Figure 3.34: 90° hybrid in circular shape

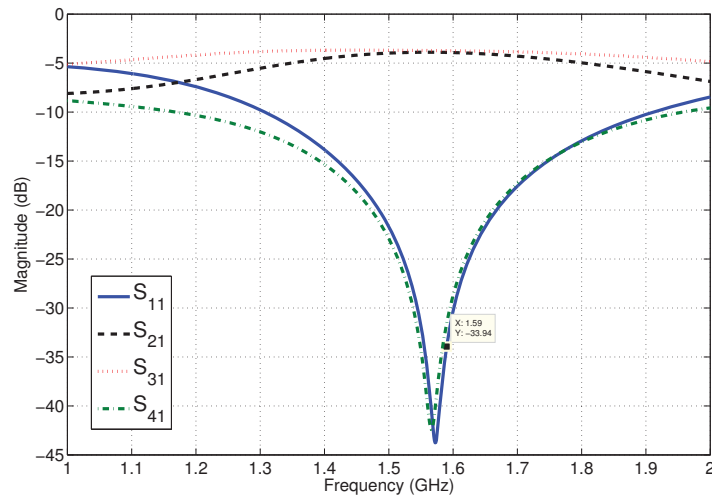


Figure 3.35: Simulation results for the S -parameters of the 90° hybrid shown in Figure 3.34

In the next step, the power divider is combined with the antenna. The patch antenna is excited at point 15mm from center of the patch for the patch radius of 25mm . The CAFSS affects the impedance of the patch antenna and hence the resonance frequency and thus,

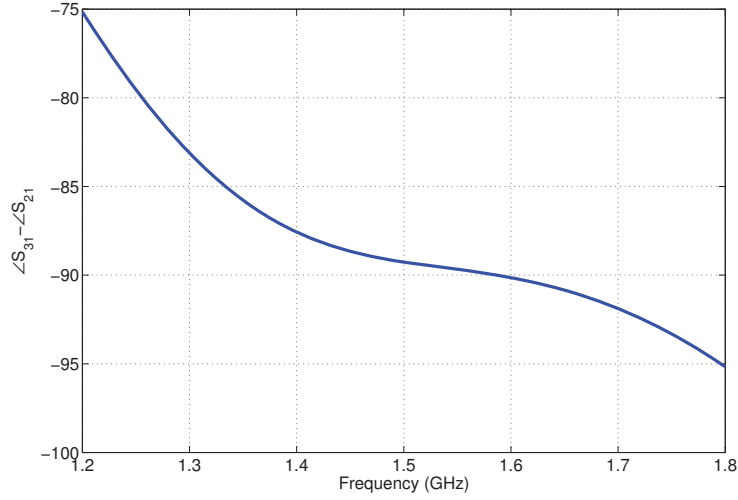


Figure 3.36: Transmission phase difference between ports 2 and 3

these parameters are derived by tuning the parameters. S -parameters of the final structure is shown in Figure 3.37. 90° hybrid is combined with the patch antenna and CAFSS with port 1 defined as the input port of the power divider and port defined as the isolated port of the power divider (see Figure 3.38). At the resonance frequency of the patch antenna, the input impedance of the antenna is 50Ω and thus power transmits to the input ports of the patch antenna and no power goes through the isolated port of the 90° hybrid.

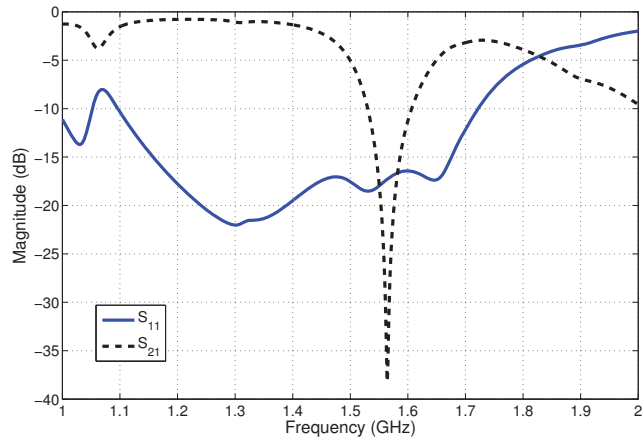


Figure 3.37: S -parameters of the 90° hybrid combined with the antenna and CAFSS

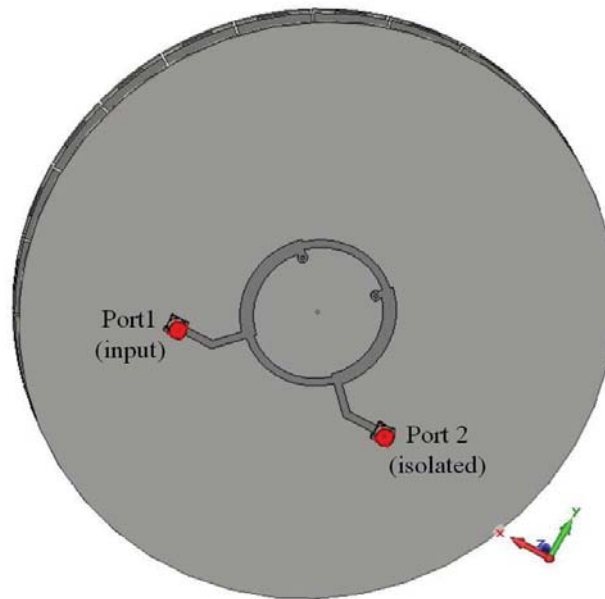


Figure 3.38: Back side view of the final structure; power divider combined with the antenna and CAFSS.

3.10 Conclusion

In this chapter, one of the problems with current GPS antennas was discussed. While the problem has been assumed to be primary due to the radiation of surface waves reaching the edges of the ground plane, it was shown that there is another important factor playing role in the corruption of AR at angles close to 90° . It was shown that this factor is an intrinsic factor of the structure which is caused by the basic radiation equations for an arbitrary antenna aperture radiating fields into the space. In this chapter, the approach to the problem was to introduce an FSS on the top of the patch antenna to form the E_θ and E_ϕ components of the fields radiated by the patch antenna. The FSS was placed in the reactive region of the antenna (a sphere of radius of about $90mm$ around the antenna for the dimensions given in this chapter) to keep the profile of the antenna small and still appropriate for many contemporary applications. Although the goal was to introduce a factor of $\cos \theta$ to the E_θ component, the CAFSS can be adequately tuned to achieve the best profile for the radiated fields to achieve the best AR at all of the planes and not necessarily the $\cos \theta$ profile. Obviously, the CAFSS presented in this chapter is not limited to the GPS application. The

approach presented can be easily applied to all the other applications requiring shaping the radiated fields of an antenna or an aperture before reaching the far-field region. Moreover, the method can be implemented in various shapes like CAFSS, RAFSS, and SAFSS (Spherically Arranged FSS) , depending on the geometry of the problem and form of the radiated fields.

In this solution, the focus was only placed to solve for the intrinsic factor in the radiated field and surface wave suppression was neglected. However, the solution is still promising even though radiation from surface waves still exists. In the next efforts, the CAFSS may be appropriately designed to exhibit band-gap properties besides its transmission properties so as to suppress the radiation from the surface waves. The result of such modification will most probably be reduction of back lobe radiation of the antenna as the diffracted waves from the edge of the ground planes are responsible for the reception from back of the antenna.

The structure can be simply implemented in various applications as it is excited on its back from one port and matched at the other port of the power divider.

Chapter 4

Conclusion and Future Work

In this chapter, we first summarize the contributions of this dissertation and conclude our work. Then, new problems are described for future research directions.

4.1 Overall Contributions

This dissertation discussed two separate, however relevant, problems with the contemporary antennas radiating CP wave. The approach to both of the problems was to integrate the antenna with FSS structure. While these structures are conventionally used as spatial filters for plane wave incidence, in this thesis, these structures are manipulated to both behave as a spatial filter and shape the radiated field of the antenna. This shaping can either be in magnitude or phase or both the magnitude and phase of the waves passing through the FSS. For the two applications of FSS discussed in this thesis, phase or magnitude of the transmitted wave is altered to achieve the desired behaviour. Although these two parameters cannot be changed and kept uncorrelated, the goal is to adjust one while keeping the changes of the other so that it does not result in huge changes of the desired radiation properties of the antenna.

4.1.1 Bidirectional Same Sense CP Wave Antenna

As discussed in Chapter 2, a bidirectional CP slot antenna was combined with the PCS. While the antenna radiates different senses of polarizations on each side, it radiates same sense of polarization on both sides of the ground plane when combined with the PCS. The role of the PCS in fact is to change the sense of the polarization as it passes through the PCS. To do so, the phase of the transmitted wave is adjusted while other parameters of the

wave is remained unchanged. The phase change discussed in this chapter is limited to 180° phase shift for one of the two perpendicular polarizations incident on the FSS. Since both the thickness and periodicity of these structures are much smaller than the wavelength, it is harder to attain other values for the change in the phase of the transmitted wave except for tiny values of phase change added to the 0° or 180° phase change of the wave by changing the physical parameters of the PCS. It should be kept in mind that the PCS is still required to demonstrate transparency at the desired frequency and not to introduce considerable loss to the transmitted wave unless it is purposefully demanded.

For the JC slot PCS presented in Chapter 2, other applications can also be imagined for other types of polarizations besides the CP wave application discussed in this thesis. For instance, for a linearly polarized (LP) wave incident on the PCS with the direction of the polarization inclined by 45° along the two directions of the PCS, with the same parameters of the PCS, the transmitted wave will undergo a rotation of the direction of polarization by 90° as a result of 180° phase change for one of the two linear polarizations along the PCS axes.

For the purpose that the antenna is designed, the structure is needed to be kept as small as possible and since the frequency of operation is within the L-band (1.575GHz), the wavelength of the wave is about 20cm. Thus the PCS is required to be placed at the close proximity of the antenna (reactive region). To exhibit the same transmission properties of PCS for higher angles of wave incidence, JC slot FSS is chosen as it is stable with regard to the angle of incidence at the angles up to 70° . Although there are many simplifying assumptions associated with the design procedure discussed in this thesis, the final simulation and measurement result are a demonstration of proof for the validity of the design procedure presented. An appropriate analytical model unifying the effect of both the FSS and the antenna, however, can help us in improving the radiation properties of the final structure.

4.1.2 Antennas with Low Susceptibility to Low Angles

Chapter 3, discussed an application of FSS for the GPS antennas for which the axial ratio is needed to be improved at the angles close to 90° off the broadside direction. Again, to keep the whole structure as small as possible, the FSS is placed at the reactive region of the antenna. In contrast to the application discussed in the previous section for changing the phase of the transmitted wave, this chapter discussed changing the magnitude of the trans-

mitted wave versus different angles waves incident on the FSS. In other words, the FSS is tapered for different angles of wave incidence. The goal was to address one of drawbacks associated with current GPS antennas. As discussed in Chapter 3, to diminish the effect of one of the factors intrinsic in radiation equations responsible for the corruption of axial ratio at low angles, magnitude of the radiated field of the antenna was manipulated differently for the two perpendicular linear polarizations before reaching far-field region of the antenna. Again, with all of the assumptions made for designing the final structure, simulation results of the axial ratio of the antenna demonstrate the validity of the procedure given to design the FSS.

As mentioned in Chapter 3, the problem is assumed to be solely due to the radiation of surface waves at the edges of the ground plane and generated by the patch antenna. Solutions available in the literature are based on suppression of surface waves. Our approach to the problem, however, was to adjust radiated fields of the antenna and the effect of the surface waves was ignored. Although the final result is still promising even with the existence of surface waves, suppressing the radiation of surface waves can improve the efficiency of the antenna further especially back-lobe radiation of the antenna which is the direct consequence of the diffracted fields at the edges of the ground plane.

The procedure presented in Chapter 3 for designing the CAFSS is based on the assumption that the CAFSS and RAFSS behave similarly in terms of transmission properties. This approach was chosen because analytical model available for the RAFSS cannot be simply applied to CAFSS as the properties and boundary conditions of the FSS changes as we move along the radius the CAFSS. Moreover, simulation setup with periodic boundary condition cannot be deployed to simulate CAFSS. Thus, although the design of the CAFSS requires more accurate and better analytical and simulation setup, existence of such models can evidently improve the final results and also ease of whole structure design. With the presence of such model, however, the mutual effect of the antenna and the FSS still is needed to be considered adequately.

4.2 Future Research Directions

While there have been a great deal of research on the FSS structures and their application in literature, most of the efforts have been on the frequency response of the FSS and also power handling capability of the FSS. As demonstrated in this thesis, however, the FSS can

be combined with the radiating element to alter the radiation properties of the antenna and derive interesting features out of the final structure. Thus, this set of structures can open a new window in addressing current limitations in the contemporary wireless and satellite systems. In what follows, a few of the research problems will be defined for future studies.

4.2.1 Dual-band Bidirectional Same Sense CP Antenna

The structure presented in Chapter 2 is designed to work at single frequency band. Many of the current systems, however, require an antenna to perform at multiple frequency bands. As discussed in Chapter 2, the FSS was designed to exhibit 0° and 180° phase shifts for the two perpendicular polarizations in order to change the sense of the polarization. As implied in that chapter, for an FSS exhibiting multiple resonance frequencies (for LP wave incidence), as we move from one resonance frequency to the next one, a phase shift of 180° will be added to the transmission phase of the wave passing through the FSS. Hence, it might seem impossible to attain a phase shift of 0° for transmission phase of one of the LP waves and 180° for the other LP wave at two frequencies. As long as the change of the sense of the CP wave is important, the property can be achieved by introducing the 0° and 180° for the two LP waves at the two frequencies interchangeably. In other words, if the FSS exhibits 0° and 180° shifts for x -directed LP wave for instance at the lower and upper frequencies, respectively, it should demonstrate 180° and 0° phase shifts at the lower and upper frequencies, respectively, for the y -directed LP wave passing through the FSS.

Designing such structure, however, requires larger FSS as a third resonance frequency is needed to design for both of the frequencies. But the FSS is not limited to JC slot FSS and any other shapes of FSS (either resonant or non-resonant) that best fits the requirements of the system can be used to design the FSS.

4.2.2 Dual-band CP Antenna with Low Susceptibility to Low Angles

Similar to dual-band bidirectional antenna, the structure discussed in Chapter 3 can also be designed for two frequencies as it is required by the antennas operating at GPS L1 and L2 bands. Since the proposed FSS is non-resonant, more layers of capacitive and inductive layers will be required to exhibit double resonance frequencies. Increasing number of layers of the FSS may result in undesired angular dependency of FSS as a result of close proximity of the antenna and the FSS. Important hint in the design of the FSS is to appropriately taper

the FSS so that it exhibits the same angular dependency at both of the resonance frequencies.

4.2.3 Surface Wave Suppressed Antenna with Improved Axial Ratio

One of the potential future research works could be an extension to the work done at Chapter 3. As discussed, for the structure presented, unlike the precedent works in this field, only the intrinsic factor present in the radiation equations was modified and there was no focus on the surface waves. Mitigating the effect of surface waves radiation at the edges of the ground plane, however, can improve the antenna performance in terms of axial ratio, susceptibility to surrounding area, and back-lobe radiation. Among various methods present in literature for removing the radiation by the surface waves, two methods can be applied to the combination of the antenna and CAFSS presented in Chapter 3. One is to stop antenna from generating surface wave modes by appropriately design the patch antenna (increasing the size of the patch and introduce vias at the required radius), as discussed in details in [23]. Other method is to introduce a periodic structure beside the antenna which exhibits bandgaps at the frequency of operation and thus can stop propagation of surface waves at the boundary of the dielectric and free space. To do so, either a separate periodic structure (basically EBG), in addition to the CAFSS, can be designed with the appropriate bandgap behaviour or the CAFSS may be modified to exhibit band-gap property for the propagation of surface waves along its interface with free space in addition to its basic property of being transparent for the propagation of antenna radiated fields and demonstrate the desired dependency versus angle of incidence. Either of the suggested methods has its own challenges. The former increases the complexity of the whole structure which elaborates the both the design procedure and the simulation process. The latter, even though with the less level of complexity, requires adequate model and design procedure to exhibit both of the aforementioned properties simultaneously.

4.2.4 Analytical Modeling of CAFSS and FSS Placed Close to the Antenna

As a general future work, deriving analytical model of each of the structures discussed in previous chapters can obviously improve the final performance of the structure. The FSS structures discussed in this thesis are designed assuming plane wave incidence. The simulations are done using periodic boundary condition which the excitation is also based on

plane wave incidence. The deployment of the FSS, however, is in reactive region of the antenna; the spot where the plane wave incidence may not be valid. Although the FSS presented in Chapter 2 can be modeled using lumped element equivalent network, the mutual effects of the FSS and the antenna is needed to be considered separately. Being close to the antenna, the FSS has a great effect on both the input impedance and radiation properties of the antenna. Hence, existence of such model can help us improve the performance of the structure presented in Chapter 2.

For the CAFSS combined with the antenna, however, the process of modeling the structure is more complicated since the FSS is arranged in cylindrical format. Besides the mutual effect of the antenna and FSS mentioned in previous paragraph, the CAFSS also needs to be modeled for cylindrical wave incidence. A similar method to [37, 38] may be used to analyze the CAFSS. But it should be pointed out that in these references the structure is designed under the surface wave propagation assumption. For our case, however, the CAFSS is excited by plane wave from bottom of the CAFSS and unlike surface waves, the propagation direction has component along the normal vector of the CAFSS plane. Consequently, those approaches cannot be directly applied to our problem and more considerations are required to appropriately model the CAFSS.

Bibliography

- [1] B. A. Munk, *Frequency selective surfaces: theory and design*. John Wiley & Sons, 2005.
- [2] M. A. Al-Joumayly and N. Behdad, "A generalized method for synthesizing low-profile, band-pass frequency selective surfaces with non-resonant constituting elements," *Antennas and Propagation, IEEE Transactions on*, vol. 58, no. 12, pp. 4033–4041, 2010.
- [3] C. A. Balanis, *Antenna theory: analysis and design*. John Wiley & Sons, 2012.
- [4] D. M. Pozar, *Microwave engineering*. John Wiley & Sons, 2009.
- [5] S. Bickel and R. Bates, "Effects of magneto-ionic propagation on the polarization scattering matrix," *Proceedings of the IEEE*, vol. 53, no. 8, pp. 1089–1091, 1965.
- [6] C. A. Balanis and J. Wiley, *Advanced engineering electromagnetics*. Wiley Online Library, 2012, vol. 111.
- [7] B. R. Rao, W. Kunysz, R. Fante, and K. McDonald, *GPS/GNSS Antennas*, 2013.
- [8] G. V. Trentini, "Partially reflecting sheet arrays," *Antennas and Propagation, IRE Transactions on*, vol. 4, no. 4, pp. 666–671, 1956.
- [9] J. Perruisseau-Carrier, "Dual-polarized and polarization-flexible reflective cells with dynamic phase control," *Antennas and Propagation, IEEE Transactions on*, vol. 58, no. 5, pp. 1494–1502, 2010.
- [10] T. N. Chang and J. Chaou, "Tapered partially reflective surface antenna," in *Antennas and Propagation Society International Symposium, 2007 IEEE*. IEEE, 2007, pp. 369–372.
- [11] S.-K. Lin and Y.-C. Lin, "A compact outer-fed leaky-wave antenna using exponentially tapered slots for broadside circularly polarized radiation," *Antennas and Propagation, IEEE Transactions on*, vol. 60, no. 6, pp. 2654–2661, 2012.
- [12] Y.-F. Lin, H.-M. Chen, F.-H. Chu, and S.-C. Pan, "Bidirectional radiated circularly polarised square-ring antenna for portable rfid reader," *Electronics Letters*, vol. 44, no. 24, pp. 1383–1384, 2008.
- [13] H. Iwasaki, "A back-to-back rectangular-patch antenna fed by a cpw," *Antennas and Propagation, IEEE Transactions on*, vol. 46, no. 10, pp. 1527–1530, 1998.
- [14] —, "Slot-coupled back-to-back microstrip antenna with an omni-or a bi-directional radiation pattern," *IEE Proceedings-Microwaves, Antennas and Propagation*, vol. 146, no. 3, pp. 219–223, 1999.

- [15] Z. Qian-yue, W. Guang-ming, and X. Dong-yu, "Bidirectional circularly polarized microstrip antenna fed by coplanar waveguide," in *Antennas, Propagation & EM Theory, 2006. ISAPE'06. 7th International Symposium on.* IEEE, 2006, pp. 1–3.
- [16] A. Narbudowicz, X. Bao, and M. Ammann, "Bidirectional circularly polarized microstrip antenna for gps applications," in *Antennas and Propagation Conference (LAPC), 2010 Loughborough.* IEEE, 2010, pp. 205–208.
- [17] Y. Zhao, K. Wei, Z. Zhang, and Z. Feng, "A waveguide antenna with bidirectional circular polarizations of the same sense," 2013.
- [18] M. Euler, V. Fusco, R. Cahill, and R. Dickie, "325 ghz single layer sub-millimeter wave fss based split slot ring linear to circular polarization convertor," *Antennas and Propagation, IEEE Transactions on*, vol. 58, no. 7, pp. 2457–2459, 2010.
- [19] M.-A. Joyal and J. Laurin, "A cascaded circular-polarization-selective surface at k band," in *Antennas and Propagation (APSURSI), 2011 IEEE International Symposium on.* IEEE, 2011, pp. 2657–2660.
- [20] J. Ashjaee, V. S. Filippov, D. V. Tatarnikov, A. V. Astakhov, and I. V. Sutjagin, "Dual-frequency choke-ring ground planes," Aug. 21 2001, uS Patent 6,278,407.
- [21] J. Tranquilla, J. Carr, and H. M. Al-Rizzo, "Analysis of a choke ring groundplane for multipath control in global positioning system (gps) applications," *Antennas and Propagation, IEEE Transactions on*, vol. 42, no. 7, pp. 905–911, 1994.
- [22] R. Baggen, M. Martínez-Vázquez, J. Leiss, S. Holzwarth, L. S. Drioli, and P. de Maagt, "Low profile galileo antenna using ebg technology," *Antennas and Propagation, IEEE Transactions on*, vol. 56, no. 3, pp. 667–674, 2008.
- [23] L. I. Basilio, R. L. Chen, J. T. Williams, and D. R. Jackson, "A new planar dual-band gps antenna designed for reduced susceptibility to low-angle multipath," *Antennas and Propagation, IEEE Transactions on*, vol. 55, no. 8, pp. 2358–2366, 2007.
- [24] S. Genovesi, F. Costa, and A. Monorchio, "Low-profile array with reduced radar cross section by using hybrid frequency selective surfaces," *Antennas and Propagation, IEEE Transactions on*, vol. 60, no. 5, pp. 2327–2335, 2012.
- [25] N. Behdad, "A second-order band-pass frequency selective surface using nonresonant subwavelength periodic structures," *Microwave and Optical Technology Letters*, vol. 50, no. 6, pp. 1639–1643, 2008.
- [26] K. Sarabandi and N. Behdad, "A frequency selective surface with miniaturized elements," *Antennas and Propagation, IEEE Transactions on*, vol. 55, no. 5, pp. 1239–1245, 2007.
- [27] P. C. Werntz and W. L. Stutzman, "Design, analysis and construction of an archimedean spiral antenna and feed structure," in *Southeastcon'89. Proceedings. Energy and Information Technologies in the Southeast., IEEE.* IEEE, 1989, pp. 308–313.
- [28] P. Mousavi, B. Miners, and O. Basir, "Wideband l-shaped circular polarized monopole slot antenna," *Antennas and Wireless Propagation Letters, IEEE*, vol. 9, pp. 822–825, 2010.
- [29] K.-L. Wong, C.-C. Huang, and W.-S. Chen, "Printed ring slot antenna for circular polarization," *Antennas and Propagation, IEEE Transactions on*, vol. 50, no. 1, pp. 75–77, 2002.

- [30] P. Hall, J. Dahele, and J. James, "Design principles of sequentially fed, wide bandwidth, circularly polarised microstrip antennas," in *Microwaves, Antennas and Propagation, IEE Proceedings H*, vol. 136, no. 5. IET, 1989, pp. 381–389.
- [31] F. Khosravi and P. Mousavi, "Bidirectional same sense circularly polarized slot antenna using polarization converting surface," *Accepted for publication in Antenna and Wireless Propagation Letters*, 2014.
- [32] —, "Bidirectional rhcp antenna using jursalem-fss polarization converter," *Antennas and Propagation (APSURSI), 2013 IEEE International Symposium on*, pp. 470–471, 2013.
- [33] I. Anderson, "On the theory of self-resonant grids," *Bell System Technical Journal*, vol. 54, no. 10, pp. 1725–1731, 1975.
- [34] R. E. Collin, "Foundations for microwave engineering," 1992.
- [35] O. Luukkonen, C. Simovski, G. Granet, G. Goussetis, D. Lioubtchenko, A. V. Raisanen, and S. A. Tretyakov, "Simple and accurate analytical model of planar grids and high-impedance surfaces comprising metal strips or patches," *Antennas and Propagation, IEEE Transactions on*, vol. 56, no. 6, pp. 1624–1632, 2008.
- [36] *IEEE standard definitions of terms for antennas*. IEEE Std 145 - 1993.
- [37] A. Sutinjo, M. Okoniewski, and R. H. Johnston, "A holographic antenna approach for surface wave control in microstrip antenna applications," *Antennas and Propagation, IEEE Transactions on*, vol. 58, no. 3, pp. 675–682, 2010.
- [38] G. Minatti, F. Caminita, M. Casaletti, and S. Maci, "Spiral leaky-wave antennas based on modulated surface impedance," *Antennas and Propagation, IEEE Transactions on*, vol. 59, no. 12, pp. 4436–4444, 2011.